

1
2
3
4
5
6
7
8
9
10
11
12
13
14
15
16
17
18
19
20
21
22
23
24
25
26
27
28
29
30
31
32
33
34
35

Targeted high throughput mutagenesis of the human spliceosome reveals its *in vivo* operating principles

Irene Beusch¹, Beiduo Rao¹, Michael Studer², Tetiana Luhovska², Viktorija Šukytė², Susan Lei¹, Juan Oses-Prieto³, Em SeGraves¹, Alma Burlingame³, Stefanie Jonas², Hiten D. Madhani^{1,4}

¹Dept. of Biochemistry and Biophysics, University of California, San Francisco, San Francisco, United States of America

²Institute of Molecular Biology and Biophysics, Department of Biology, ETH Zurich, Zurich, Switzerland

³Dept. of Pharmaceutical Chemistry, University of California, San Francisco, San Francisco, United States of America

⁴hitenmadhani@gmail.com

36 **SUMMARY**

37

38 The spliceosome is a staggeringly complex machine comprising, in humans, 5 snRNAs and
39 >150 proteins. We scaled haploid CRISPR-Cas9 base editing to target the entire human
40 spliceosome and interrogated the mutants using the U2 snRNP/SF3b inhibitor, pladienolide B.
41 Hypersensitive substitutions define functional sites in the U1/U2-containing A-complex but also
42 in components that act as late as the second chemical step after SF3b is dissociated. Viable
43 resistance substitutions map not only to the pladienolide B binding site but also to the G-patch
44 (ATPase activator) domain of SUGP1, which lacks orthologs in yeast. We used these mutants
45 and biochemical approaches to identify the spliceosomal disassemblase DHX15/hPrp43 as the
46 ATPase ligand for SUGP1. These and other data support a model in which SUGP1 promotes
47 splicing fidelity by triggering early spliceosome disassembly in response to kinetic blocks. Our
48 approach provides a template for the analysis of essential cellular machines in humans.

49

50 INTRODUCTION

51 Pre-mRNA splicing is an essential step in eukaryotic gene expression. In addition to
52 driving proteome diversity via alternative splicing (Blencowe, 2017), splicing impacts RNA
53 stability, for example through the inclusion of exons with premature termination codons subject
54 to nonsense-mediated decay (NMD), and plays critical roles in RNA export and translation
55 efficiency (Le Hir et al., 2016). Splicing is also a major player in human disease: a large fraction
56 of single nucleotide polymorphisms associated with human disease impact splicing (Li et al.,
57 2016), and many human cancers harbor driver mutations in components of the spliceosome
58 itself (Bejar, 2016; Yoshimi et al., 2019)

59 There are four intron sequences important for splicing: the 5' splice site (SS), the
60 branchpoint (BP), the polypyrimidine tract (PPT), and 3' splice site (Fig. 1). In humans, there is
61 large variability in these sequences, which can have an enormous impact on splicing efficiency
62 and regulation, enabling regulation by RNA binding proteins (RBPs). Pre-mRNA splicing
63 proceeds via two transesterification reactions which are catalyzed by the spliceosome.
64 Compared to the simplicity of the chemical steps, the spliceosome is staggeringly complex
65 (Figure 1 A,B). Components include five small nuclear ribonucleoproteins (snRNPs – U1, U2,
66 U4/U6, and U5) and numerous proteins that assemble onto the intron substrate and undergo
67 several large rearrangements to form a catalytically active complex in which a U6 snRNA acts
68 as an RNA catalyst (Wilkinson et al., 2020). In *S. cerevisiae*, from which much of our
69 understanding has been developed, splicing of a single intron requires eight ATP-dependent
70 steps and about 90 proteins. Human spliceosomes appear to contain about 60 additional
71 proteins (Wahl et al., 2009a).

72 Initial intron recognition involves base-pairing between the 5' end of U1 snRNA and the
73 5' SS and recognition of the branchpoint, PPT, and 3' SS by sequence-specific RNA binding
74 proteins: Splicing Factor 1 (SF1/Msl5) recognizes the branchpoint sequence while the two
75 subunits of U2AF recognize the PPT and the conserved AG dinucleotide at the 3' splice site.
76 This forms an early, or E, complex that is the precursor to the A complex in which U2 snRNP
77 binds to the intron, base-pairing with sequences around the branchpoint (the branchpoint
78 sequence), replacing SF1 and U2AF. A triple snRNP, containing base-paired U4/U6 snRNAs

79 together with the U5 snRNA, then joins the complex to form the pre-B complex which converts
80 to the B complex by the departure of U1. Activation of the spliceosome occurs via ATP-
81 dependent rearrangements that expels the U4 snRNP and several proteins (Wahl et al.,
82 2009b), allowing the PRPF19/Prp19 complex (NTC) and NTC-related proteins (NTR) to join.
83 This produces the B^{act} complex, in which U6 base-pairs with the 5' splice site and U2 and U6
84 snRNAs base-pair to form the spliceosomal active site (Wilkinson et al., 2020). A component of
85 U2 snRNP, the SF3 complex, which sequesters the U2-branchpoint helix away from the 5'
86 splice site, is then removed, allowing the U2-branchpoint helix to dock with the catalytic core.
87 Association of additional proteins allow the chemical steps to proceed in the B* and C* catalytic
88 complexes (Wilkinson et al., 2020). The ATPases DHX38/Prp16 and DHX8/Prp22 respectively
89 remodel the active site after each chemical step (Wahl et al., 2009b). Following mRNA release,
90 the helicase DHX15/Prp43 disassembles the spliceosome (Martin et al., 2002; Tsai et al.,
91 2005). Like other DEAH-box helicases, DHX15/Prp43 is activated by a cognate G-patch
92 protein, TFIP11/Spp382/Ntr1 (Tanaka et al., 2007).

93 Given the high variability in splicing signal sequences in humans, how the spliceosome
94 distinguishes between cognate and noncognate sequences remains to be understood. A
95 longstanding hypothesis suggests that the dynamic and complex nature of the spliceosome
96 promotes the fidelity of splicing through kinetic proofreading while also permitting substrate
97 flexibility and regulation. Evidence supporting this model came from a genetic screen in *S.*
98 *cerevisiae* in which missense mutations in the ATPase Prp16 were identified as suppressors of
99 a mutation in the branchpoint adenosine sequence (Burgess and Guthrie, 1993). Subsequent
100 *in vitro* studies demonstrated that mutant pre-mRNA substrates that assemble into
101 spliceosomes, but are kinetically slow at either chemical step, trigger spliceosome disassembly
102 prior to completion of the reaction, a process termed “discard” (Koodathingal et al., 2010;
103 Koodathingal and Staley, 2013; Mayas et al., 2010; Mayas et al., 2006; Semlow and Staley,
104 2012). Failure to perform catalysis prior to ATP hydrolysis by Prp16 (step 1) or Prp22 (step 2)
105 produces a spliceosome that can be disassembled by Prp43. These ATPases have been
106 proposed to act as molecular timers for productive movement through the splicing pathway
107 (Koodathingal and Staley, 2013). The yeast studies used mutant pre-mRNA substrates

108 because their signals are always very close to the optimal consensus (Irimia and Roy, 2008).
109 Whether there are analogous or additional fidelity mechanisms that operate in animal cells is
110 unknown.

111 The ability to perform forward genetic screens in haploid *S. cerevisiae* was critical for
112 the studies on spliceosome fidelity outlined above as well as numerous other foundational
113 studies of splicing. To adapt these methods to human cells, we describe here a strategy to
114 mutagenize the spliceosome in fully haploid human cells by developing and deploying a
115 CRISPR-Cas9 base editor sgRNA library that targets the entire human spliceosome. After
116 mutagenesis, we interrogated the spliceosome using the potent inhibitor pladienolide B (PB),
117 which targets U2 snRNP by binding to a pocket between the SF3B1 and PHF5A subunits of the
118 SF3b complex, preventing stabilization of the U2-branchpoint RNA duplex (Cretu et al., 2018b;
119 Cretu et al., 2021; Gamboa Lopez et al., 2021; Teng et al., 2017b; Wu et al., 2018). Validation
120 and genomic sequencing revealed resistance mutations in SF3B1 and PHF5A in residues
121 adjacent to the compound binding pocket. We mapped hypersensitive mutants to U2 snRNP
122 components, but also to factors that act as late as the second chemical step, after SF3b has
123 dissociated. Strikingly, we obtained resistance mutants in SUGP1, a spliceosomal G-patch
124 protein of unknown function that lacks orthologs in yeast and is also a newly proposed tumor
125 suppressor whose loss underpins the splicing changes induced by cancer-associated SF3B1
126 mutations (Alsafadi et al., 2021; Liu et al., 2020; Zhang et al., 2019). Our resistance mutations
127 in SUGP1 map in or adjacent to its G-patch motif and modulate splicing changes triggered by
128 PB. We describe biochemical experiments that reveal the spliceosomal disassembly ATPase
129 DHX15/hPrp43 to be the biologically relevant direct target of the SUGP1 G-patch domain. We
130 propose a unified model in which SUGP1/DHX15-mediated disassembly of kinetically-slowed
131 early splicing complexes explains compound resistance as well as oncogenic aberrant splicing
132 events resulting from SF3B1 and SUGP1 mutations. More broadly, our results demonstrate the
133 feasibility and utility of the programmed generation of informative viable haploid alleles
134 targeting a complex essential gene expression machine in human cells.

135

136

137 RESULTS

138 Large-scale mutagenesis of the human spliceosome

139 A major impediment to the study of the human spliceosome *in vivo* has been the
140 inability to program point mutations in endogenous genes on a large scale. CRISPR-Cas9
141 technology now provides such opportunities (Anzalone et al., 2020). Due to its scalability and
142 ability to introduce point mutations, we chose CRISPR-Cas9 base editing for a forward genetic
143 screen of the spliceosome (Figure S1B). We first generated a monoclonal stable cell line
144 expressing FNLS (Zafra et al., 2018a), a cytosine base editor, in an eHAP (Essletzbichler et al.,
145 2014) haploid cell background (hereafter: eHAP FNLS). During clonal cell line generation, we
146 maintained eHAP FNLS cells as haploid so that we could subsequently assign genotype-
147 phenotype relationships (Figure 1D). We assessed editing efficiency on a set of standard
148 targets used previously (Zafra et al., 2018b) (Figure S1C,D). eHAP FNLS cells demonstrated
149 efficient editing (up to >90%) at expected positions within the editing window, which spans
150 positions 3-8 [with position 21-23 being the protospacer adjacent motif (PAM)], and induced
151 transversions (C > R editing) at high frequencies (>25%) in some cases. Transversion editing
152 has been described previously; its extent is cell line-dependent (Sánchez-Rivera et al., 2022) .

153 We designed a single guide RNA (sgRNA) library targeting a hand-curated list of 153
154 human spliceosomal proteins which engage at various steps of the splicing cycle (Figure 1A),
155 and are reproducibly detected through mass spectrometry (MS), interaction studies, and/or
156 visualized in structural biology studies (see Figure 1B, Table S1)(Sales-Lee et al., 2021) .
157 Given that base editing outcomes are not fully predictable, to maximize mutagenesis we
158 targeted every available NGG PAM sequence across all annotated exons plus 20 bp flanking
159 intronic sequence (Figure 1C). Our library includes 42,618 sgRNAs targeting 42,650 sites,
160 including 8,426 sgRNAs that target genomic sites but are predicted to be non-editing with
161 FNLS, and an additional 1,000 guides that do not target genomic sites (non-targeting sgRNAs)
162 (Doench et al., 2016) . The library can in principle mutagenize up to 30% of spliceosomal
163 protein coding sequences (Figure S1E) and edits are predicted to result in in missense

164 mutations in >50% of cases with an additional 20% of edits predicted to impact protein
165 sequence (Figure S1F, and Methods for details on mutation outcome prediction).

166 We cloned this library into lentiviral vectors that express the sgRNA and associate each
167 to a unique barcode and produced virus for transduction (Figure S1A) (Boettcher et al., 2019).
168 We transduced the library into eHAP FNLS cells, incubated them for 6 days to allow for editing
169 and selection of transduced cells, and then split the selected pool into treatment arms
170 (control/DMSO vs. 2 nM PB, which approximates its EC₅₀). We cultured cells for two weeks
171 while maintaining a representation of 500 cells per sgRNA. On days 0, 8 and 14 we isolated
172 genomic DNA and amplified and sequenced the sgRNA inserts; we also did this for the input
173 plasmid library (Figure 1E). Using the sgRNA-linked barcode, we randomly assigned sgRNAs
174 to two sample populations and depletion vs. enrichment of sgRNAs was analysed for both time
175 and treatment using DESeq2 (Love et al., 2014).

176 We then compared the abundances of guide sequences in the population that differed
177 in their predicted consequences versus the plasmid input control 14 days after transduction.
178 Given that most spliceosomal proteins are essential for cell survival, we anticipated that a
179 subset of induced mutations would be lethal or result in reduced viability, and that their sgRNAs
180 would therefore be depleted over time. As expected, sgRNAs predicted to promote mutations
181 with more severe consequences such as splice site mutations or creation of stop codons
182 displayed the strongest depletion as a class, consistent with efficient and precise editing at
183 many of those sites (Figure S1G). Conversely, guides predicted to be non-editing or to produce
184 silent mutations were generally not depleted

185 By comparing guide sequence abundances for day 14 for 2 nM PB versus the matched
186 DMSO control, we observed that several guides were enriched or depleted upon compound
187 treatment of the population (Figure 1F). For validation, we selected the sgRNAs showing
188 statistically significant enrichment or depletion (LFC > |2|, padj < 0.05) between the 2 nM PB
189 sample and its matched control sample on day 14. To this list we added a subset of sgRNAs
190 with high average enrichment/depletion but did not pass statistical significance (see Methods
191 for details). To enrich for PB-specific phenotypes, we required that those guides depleted after
192 PB treatment did not show depletion between t0 and t14 in untreated cells. This procedure

193 yielded 19 candidate-enriched sgRNAs and 26 candidate-depleted sgRNAs. These sgRNAs
194 and three non-targeting sgRNAs were then subjected to an arrayed dual-color competition
195 assay in which cells transduced with virus encoding a non-targeting sgRNA or transduced with
196 a candidate-depleted or -enriched sgRNA were marked with distinct fluorescent proteins,
197 respectively (Figure 2A). The assay confirmed the response to PB treatment for 23/26 of the
198 candidate-depleted sgRNAs and 11/19 of the candidate-enriched sgRNAs. Except for a sgRNA
199 targeting *SF3B1* and another targeting *PRPF6*, only sgRNAs found to be statistically
200 significantly enriched validated in the confirmation assay, supporting the utility of the statistical
201 approach used (Figure 2B, S2A).

202

203 **Pladienolide B hypersensitive mutations identify functional spliceosomal residues**

204 Given the notable number of sgRNAs depleted upon compound treatment, we
205 determined the genomic consequences of base editing. We transduced eHAP FNLS with
206 lentivirus carrying individual sgRNAs, grew cells for six days, isolated genomic DNA, amplified
207 the edited locus and subjected the amplicons to deep sequencing. This approach revealed the
208 consequences of base editing at the amino acid level (Table S2).

209 Guides presumably must edit efficiently to produce a depletion phenotype. Amplicon
210 sequence confirmed this expectation: all sgRNAs displayed high/substantial rates of editing
211 (median = 57.7% for C > T within positions 3 to 8, Figure S2B) leading to amino acid changes
212 that become depleted in the presence of PB (with a median of 82% of the sequences carrying
213 an amino acid change, Table S2). Again, we observed not only C > T editing but also C > R
214 editing, with predicted mutations matching for 19/23 sgRNAs. Thirteen distinct guides
215 programmed mutations in early-acting spliceosomal factors, including SF1, SF3, and
216 DDX46/hPrp5 as well as the U2AF-associated DEAD box protein DDX5/UAP56 (Figure 2C).
217 Unexpectedly, we also identified a mutation in the tri-snRNP-specific protein USP39/hSad1 and
218 five mutations in the second-step factor CDC40/hPrp17, which is first found in the B^{act} complex
219 (Haselbach et al., 2018). Finally, we found PB-sensitive mutations in factors that join
220 catalytically active complexes and act at the second chemical step of splicing (DHX35/hPrp16
221 and CACTIN), a point in the spliceosome cycle after which SF3b has been dissociated. As a

222 first step in understanding how these changes impact the spliceosome, below we briefly place
223 some of these mutations into the context of existing spliceosome structures, focusing on the
224 SF3 complex.

225 PB sterically blocks binding of the U2-intron branchpoint duplex to its pocket in SF3b
226 (Cretu et al., 2021), which is necessary for spliceosome assembly to proceed beyond the A
227 complex. Six of our PB-sensitive mutants occur in the SF3 complex, which consists of the SF3a
228 and SF3b subcomplexes (Brosi et al., 1993) . Recent work has shown that the HEAT-repeat
229 region of SF3B1, a SF3b component, undergoes a conformational transition upon U2 snRNP
230 binding to the branchpoint, moving from an open conformation to a closed state, thereby
231 stabilizing the U2-branchpoint duplex (Tholen et al., 2022; Zhang et al., 2021; Zhang et al.,
232 2020a). We mapped an SF3B3 E159K mutant to an interface between SF3B3, SF3B1 and
233 PHF5A (Figure 2D), distal to where PB or the branchpoint engages SF3b. The mutation lies in
234 a region of SF3b that changes conformation upon binding to the branch helix (formed between
235 U2 and the branchpoint sequence) (Figure 2E), likely impacting SF3B1 closing which would
236 favor PB binding and, presumably, cell growth inhibition. Finally, we mapped PB-sensitive
237 substitutions in residues in several factors not part of SF3b onto available structures
238 (Haselbach et al., 2018; Nameki et al., 2022; Zhang et al., 2018) and found that they often
239 occur at protein-protein interfaces (Figure S3D-F, Table S2), providing a resource for structure-
240 functional studies.

241

242 **Viable SF3b mutations produce resistance to pladienolide B**

243 SF3B1 and PHF5A mutations have been identified that render cells resistant to PB
244 treatment (Cretu et al., 2018b; Teng et al., 2017a), but they only occur in a dominant
245 (heterozygous) fashion, suggesting recessive lethality. Nonetheless, in our haploid screen, we
246 identified eleven significantly enriched sgRNAs that target these factors, five against *PHF5A*
247 and one against *SF3B1*, (Figure 1F). To identify the underlying alleles, we transduced eHAP
248 FNLS cells with individual sgRNAs and collected cells at t0, t8 and t15 in the presence and
249 absence of 2 nM PB treatment. Following genomic DNA isolation and amplicon deep
250 sequencing, we determined mutation prevalence across time and treatments (Figure 3A). Note

251 that for efficient guides, resistance-promoting mutations may be highly prevalent at t0 and
252 therefore may not enrich in abundance under compound treatment (see e.g., sgPHF5A_7,
253 Figure S3A).

254 sgSF3B1_166 was the only sgRNA conferring PB resistance through mutation of
255 SF3B1. For this guide, no mutant alleles were detected by sequencing in the transduced cell
256 population in the absence of PB treatment (possibly due to poor editing efficiency), but an allele
257 encoding a T1080I change enriched rapidly upon PB addition to cells carrying this sgRNA
258 (Figure 3B). In contrast, all five guides targeting *PHF5A* gave rise to substantial cell populations
259 carrying different mutations at t0. Both sgPHF5A_7 and sgPHF5A_21 are predicted to result in
260 cysteine to tyrosine mutations for side chains involved in the coordination of a Zn²⁺ ion.
261 However, in both instances deep sequencing revealed that the predicted Cys > Tyr mutation
262 was not detected; rather, we observed mutations impacting the preceding residue (Figure
263 S3A,B). Both the resulting PHF5A K29N and E74D mutation arise through transversion (C > R
264 mutation). sgPHF5A_47 is predicted to result in mutation and loss of the 3' splice site of exon
265 3. This mutation did occur at high frequency (Figure S2C) and likely resulted in a growth
266 disadvantage (see Figure S2A, reduced fitness of sgPHF5A_47 transduced cells in absence of
267 PB). Instead, after transduction with this guide, the more frequent mutation at t0 encodes a
268 D27N change which further accumulates in the population under compound selection. The
269 remaining two resistance-promoting sgRNAs in *PHF5A* are predicted to be non-editing.
270 sgRNA_PHF5A_6 targets a cytosine at position 7 in a G₆C₇ dinucleotide context, which is
271 unfavourable to editing (Kluesner et al., 2021; Sánchez-Rivera et al., 2022). Indeed, this
272 sgRNA resulted only in 12% of amplified molecules harboring the anticipated D47N mutation.
273 Surprisingly, under PB selection, the more frequent mutation encodes a two amino acid
274 insertion (TL) between C40 and T41 producing a tandem TL dipeptide in the protein sequence
275 (hence we name the allele PHF5A-2xTL) (Figure 3C). This TL-encoding insertion occurred at
276 position -3 relative to the PAM of sgRNA_PHF5A_6 where the nCas9 of the CRISPR-Cas9
277 base editor nicks the genomic DNA upon genomic binding. For the other non-editing sgRNA,
278 sgRNA_PHF5A_26, editing should not occur within the editing window due to an absence of
279 cytosines. Indeed, we observed edits 13 and 15 bp upstream of the targeted sequence, which

280 alter S67 (Figure S3A, see Figure S3E for a summarized comparison of predicted mutations vs
281 those identified by sequencing).

282 Using this information, we mapped the encoded amino acid changes on the available
283 structures of SF3B1 and PHF5A. For SF3B1, the change lies within heat repeats 15 and 16,
284 which form a hinge region that supports a conformational change necessary for BP-A binding
285 (Figure 3D,F) (Cretu et al., 2018a; Tholen et al., 2022; Zhang et al., 2020b). This location
286 differs from those of reported resistance mutations in SF3B1 at K1071, R1074 and V1078 –
287 which are all residues that face PB in high resolution structures (Teng et al., 2017b; Yokoi et
288 al., 2011) . For PHF5A, all five mutations that we identified impact residues in a protein surface
289 near the PB binding site, where PHF5A interacts with both SF3B1 and the U2-branchpoint helix
290 (Figure 3E,F) (Tholen et al., 2022) This contrasts with the location of the reported (dominant
291 resistant) Y36C mutation, which changes a residue that directly contacts PB (Teng et al.,
292 2017b) .

293 To test whether these mutations produce resistance to concentration-dependent acute
294 killing by PB, we repeated guide transduction experiments followed by single cell cloning to
295 generate six independent monoclonal cell lines, three harboring the mutation PHF5A-2xTL and
296 three harboring SF3B1-T1080I (Figure S4A). The measured half maximal effective
297 concentration (EC_{50}) of PB in a cell viability assay at 60 h post treatment confirms that PHF5A-
298 2xTL (34 nM) and SF3B1-T1080I (24 nM) confer concentration-dependent resistance to killing
299 by PB relative to the parental cell line ($EC_{50} = 2$ nM) (Figure 3G).

300

301 **Mutations in the G-patch tumor suppressor protein SUGP1 confer PB resistance**

302 Unexpectedly, our screen identified resistance mutations in three factors, PRPF6, SF1
303 and SUGP1, that are not part of SF3b, the target of PB. We focussed on the analysis of the
304 SUGP1 mutations. *SUGP1* (SURP and G-patch domain containing 1) was targeted by two
305 guides, both of which were confirmed in competition validation assays (Figure 1F, 2B, S2A).
306 Transduction, compound treatment, and amplicon deep sequencing suggests that
307 sgSUGP1_238 produces resistance via an E554K mutation and sgSUGP1_188 produces
308 resistance via a G603N mutation (Figure 3B, C).

309 Both mutations match the editing predictions with one encoding a change lying in
310 (G603N) and the other just upstream (E554K) of the G-patch motif (Figure 3A,D). SUGP1 is
311 associates with the spliceosomal A complex, where it interacts with SF3B1 (Zhang et al.,
312 2019). SUGP1 has not yet been visualized in any spliceosome structure, nor are there
313 orthologs in *S. cerevisiae* or *S. pombe*. Recent work has identified SUGP1 as a putative tumor
314 suppressor: its loss from the spliceosome was suggested to underlie splicing and oncogenic
315 phenotypes of SF3B1 tumor mutations, and mutations in SUGP1 found in tumors mimic the
316 splicing phenotype of SF3B1 mutant tumors (Alsafadi et al., 2021; Liu et al., 2020; Zhang et
317 al., 2019).

318 For EC₅₀ assays, we again repeated transductions and produced three independent
319 monoclonal cell lines (Figure S4A) for each mutation. To our surprise, no substantial change in
320 EC₅₀ for PB was observed (Figure S4B). However, the EC₅₀ measurement occurs over a much
321 shorter time frame than treatment during the screen, which indicates that the mutations confer
322 resistance to PB-mediated growth inhibition over time but not immediately. These data suggest
323 that the SUGP1 mutants act by a mechanism distinct from those in SF3B1 and PHF5A, which
324 map near the drug binding site.

325

326 **SUGP1 mutations modulate a subset of PB-induced exon skipping events**

327 PB induces massive exon skipping as well as other splicing changes (Wu et al., 2018).
328 To investigate the impact of SUGP1 mutations on PB-induced splicing changes, we performed
329 RNA-seq analysis on our clonal cell lines. We also included the PHF5A-2xTL and SF3B1-
330 T1080 clonal cell lines. Cells were treated with DMSO or 2 nM PB (= EC₅₀) for 3 h (a time
331 frame where cell viability is not yet affected, see Figure S4C) prior to RNA extraction and
332 polyA-selection. We detected no changes in global transcript levels in the mutant cell lines
333 (Figure S4C).

334 We used rMATS (Shen et al., 2014b) to detect differential alternative splicing events. In
335 untreated cells, we observed exon skipping (skipped exon, SE) as the most frequent event
336 triggered by the mutations followed by alternative 3' splice site (A3'SS) use; relatively few
337 introns were impacted [using a difference percent splicing inclusion (Δ PSI) cut-off of \geq |10%|

338 and FDR > 0.01] (Figure 4E). Among these were changes in 3' splice site usage in introns of
339 the *TMEM14C* and *ENOSF1* genes, which, strikingly, correspond exactly to changes observed
340 previously in cells harboring SF3B1 cancer mutations or SUGP1 cancer mutations (Figure 4F,
341 G, S4D-F) (Alsafadi et al., 2021; Liu et al., 2020).

342 Upon PB treatment of these cell lines, the number of differentially spliced junctions
343 increased drastically. Control cells (eHAP FNLS transduced with a non-targeting sgRNA)
344 displayed the largest number of PB-induced splicing changes, while the PHF5A-2xTL and
345 SF3B1-T1080 showed almost no changes, as would be expected if they were to reduce the
346 effects of compound binding to the spliceosome (Figure 5A). Both SUGP1 mutants displayed
347 an intermediate phenotype with fewer affected events than wild-type in the presence of PB.

348 Focusing on A3'SS and SE events induced by PB, we observed a general concordance
349 between control cells and SUGP1 mutants (Figure 5B, C). Hierarchical clustering of the splicing
350 junctions quantified by rMATS across all samples demonstrated that PB treatment almost
351 exclusively triggered increases in exon skipping (Figure 5E), but both increases and decreases
352 use of alternative 3' splice sites (Figure 5D). Subsets of splicing events induced by PB were
353 affected either equally strongly in control and SUGP1 mutant lines (example: *RBM5* exon 16 in
354 Figure 5F, S5B) or displayed milder changes in the SUGP1 mutants (example: *ORC6* exon 5 in
355 Figure 5G, S5B, C). No statistically significant differences in intronic or exonic features at the
356 introns equally vs. differentially affected by SUGP1 genotype were identified using Matt (Gohr
357 and Irimia, 2019); thus additional work will be necessary to identify the determinants of SUGP1-
358 sensitive, PB-induced alternative splicing events. These findings demonstrate that SUGP1
359 mutants can modulate splicing changes induced by PB, as expected from the ability of SUGP1
360 to produce relative resistance to the compound.

361

362 **DHX15/hPrp43 is a mutationally sensitive ligand of the G-patch motif of SUGP1**

363 G-patch motifs (named for their glycine-richness) are direct activators of DEAH-box
364 helicases (Studer et al., 2020a; Warkocki et al., 2015); this is the only known activity of this
365 domain. SUGP1 has therefore been suggested to recruit a helicase through its G-patch motif to
366 SF3B1 and the A complex (Alsafadi et al., 2021; Liu et al., 2020; Zhang et al., 2019). As we

367 identified mutations within and just upstream of the SUGP1 G-patch, it seemed likely that one
368 or both mutations impact the association and/or activation of a cognate DEAH-box ATPase.
369 Indeed, the G603N mutation lies within the “brace loop” analogous to the only G-patch protein
370 for which its helicase-bound structure is available (Figure 4D), a region known to be important
371 for the NKRF G-patch to bind and activate its cognate DEAH box helicase DHX15 (Studer et
372 al., 2020b).

373 To identify SUGP1 helicase partner(s), we employed proximity labelling (BioID)
374 exploiting our SUGP1 G603N mutant as a control. Recent advances allow for short labelling
375 times using Turbo fusion proteins (Branon et al., 2018). After optimizing conditions, we
376 transfected HEK293T cells with expression plasmids encoding SUGP1 with a C-terminal
377 miniTurboID fusion. After a short 2 min labelling pulse with biotin, extracts were prepared, and
378 labelled proteins purified under harsh conditions using streptavidin. Replicate samples were
379 subjected to tandem mass tag mass spectrometry (TMT-MS) (Figure S6A,B) to identify
380 differentially labelled proteins. Remarkably, only a single protein displayed a statistically
381 significant reduction in signal in the SUGP1-G603N-miniTurboID-tagged samples versus those
382 obtained with the wild-type fusion: the DEAH-box helicase DHX15/hPrp43, the protein that
383 disassembles the spliceosome (Figure 6A). We also identified DHX15/hPrp43 in a parallel
384 experiment using a fusion of a SUGP1-L570E-miniTurboID fusion which we constructed based
385 on the ability of this mutation to disrupt G-patch/DEAH protein interactions for a different G-
386 patch protein, NKRF (Studer et al., 2020b) (Figure S6C).

387 To test more directly the impact of the G-patch mutations on the interaction and/or
388 activation of with DHX15, we employed biochemical methods. Modelling of a SUGP1-DHX15
389 using AlphaFold2 (Jumper et al., 2021) predicted that the G-patch domain of SUGP1 interacted
390 with DHX15 as anticipated but that the G-patch was flanked by unanticipated α -helical
391 elements that are also predicted to interact with DHX15. In this model, the E554K substitution
392 may impact a contact with the flanking α -helices (Figure 6B). We overexpressed SUGP1
393 mutants in HEK293T cells to assess their impact on splicing. We observed that deletion of α H4-
394 5 or α H6 as well as the E554K, G603N, and L570E substitutions displayed similar effects on
395 splicing (Figure S5D-G). Thus, we constructed a series of maltose binding protein (MBP) fusion

396 proteins harboring the SUGP1 G-patch and varying lengths of flanking sequences (Figures
397 6D,E and S6C).

398 We next mixed a purified version of DHX15 lacking its N-terminal domain (DHX15 Δ N)
399 with each MBP-SUGP1 fusion proteins, purified them with amylose beads, and analyzed the
400 material using SDS-PAGE. We observed that DHX15 Δ N selectively copurified with each of the
401 MBP-SUGP1 fusion proteins (Figure 6D-E and S6D). However, we found that the efficiency of
402 copurification decreased with increasing length of SUGP1 constructs, indicating that protein
403 stretches surrounding the G-patch modulate its binding affinity for DHX15. For each of these
404 constructs, we generated mutations in the G-patch, corresponding to the two obtained in our
405 screen, E554K and G603N, as well as one in the central “brace-helix”, L570E, that is known to
406 disrupt ligand binding in analogous G-patch proteins. For the construct harboring the most
407 upstream SUGP1 sequences (436-633) all mutations reduced binding to DHX15 Δ N, consistent
408 with loss of DHX15 labelling we observed in the BioID experiment. Therefore, it is likely that
409 disruption of DHX15 interaction forms the molecular basis for the observed PB resistance of
410 the SUGP1 mutants obtained in our screen. Consistent with the stronger affinity of DHX15 Δ N
411 for the intermediate [MBP-SUGP1(522-633)] and shortest [MBP-SUGP1 (548-611)] SUGP1
412 constructs, their binding was not sensitive to the mutations obtained in our screen but was only
413 disrupted by mutation of the core interface residue L570E.

414 As G-patch proteins can enhance RNA binding to DEAH-box helicases (Studer et al.,
415 2020b), we used fluorescence anisotropy to ask whether the SUGP1 fusions increased RNA
416 affinity of DHX15 Δ N. Using a fluorescently labelled poly-U RNA, we found that all SUGP1
417 constructs indeed increased RNA binding to DHX15 Δ N ~10-20-fold (Figure 6F-G and S6F). In
418 agreement with their effect on binding DHX15, all mutations in the longest SUGP1 construct
419 (436-633) blocked this stimulation (Figure 6G), while varying degrees of mutational sensitivity
420 were observed for the shorter SUGP1 truncations (Figure 6G and S6G), again indicating an
421 important role for sequences flanking the G-patch domain.

422 Finally, we investigated the ability of SUGP1 to stimulate the ATPase activity of
423 DHX15 Δ N that is required for and coupled to its RNP remodelling activity. Indeed, SUGP1
424 (548-611) produced a 1.8-fold increase in initial ATPase rates of DHX15 Δ N at saturating ATP

425 concentrations, which was significantly diminished by all mutations consistent with their
426 negative effects on DHX15 binding.

427

428

429 **DISCUSSION**

430 The human spliceosome is essential for the splicing of over 200,000 introns in the
431 human genome. Because it is mutated in numerous diseases and the target of myriad splicing
432 regulators, it is a key compound development target. Numerous questions exist regarding the
433 coupling of transcription and chromatin to splicing, the underpinnings of splicing fidelity, and the
434 functional roles of many if not most human spliceosomal proteins. However, the genetic
435 analysis of the human spliceosome has not been pursued, even though it harbors ~60 proteins
436 not found in *S. cerevisiae* and is likely to operate in ways that cannot be anticipated from prior
437 studies of yeast. Particularly useful would be so-called “informative alleles” that dissect
438 essential protein function. While CRISPR-Cas9 knockout screens are not designed to generate
439 such information, CRISPR base editing and related methods in principle provide approaches
440 generating programmed point mutations. We adapted pooled CRISPR-Cas9 base editing to the
441 human spliceosome to mutagenize 153 protein subunits in a haploid cell context. We
442 interrogated the mutants with PB, a prototype for a class of anti-cancer compounds that targets
443 the SF3b complex. Our studies provide insights into structure-function relationships by
444 identifying viable alleles of numerous spliceosomal proteins that program hypersensitivity or
445 resistance to SF3b inhibition. We demonstrate the utility of such alleles through studies of the
446 SUGP1 tumor suppressor. Below we discuss the evidence for these conclusions and propose a
447 new human-specific discard/fidelity step mediated by the activation of the spliceosomal
448 disassemblase DHX15/hPrp43 by SUGP1 during early stages of spliceosome assembly and its
449 implications for human disease.

450

451 **PB hypersensitive mutations identify functional sites in the human spliceosome that** 452 **vary in the human population**

453 We obtained PB-hypersensitive mutants in a small subset of the 153 proteins
454 mutagenized. Gratifyingly, most lie in factors that act at or near the step inhibited by PB,
455 including in SF1 and components of U2 snRNP. This specificity highlights the utility of single-
456 residue chemical-genetic interactions to identify functional sites related to a particular phase of
457 an essential process. As described in the results above, many mutations we identified could be

458 placed on existing structures, enabling the generation of structure-function relationships.
459 However, most of the residues altered in our mutants are not visualized in existing structures.
460 In both cases, detailed studies *in vitro* and/or *in vivo* will be required to understand the impact
461 of these functional sites on splicing of the numerous endogenous introns that interrupt human
462 genes. The mutations identified here provide a resource for such investigations.

463 Mutations in the second-step factor CDC40/hPrp17 and CACTIN produce PB
464 hypersensitivity to PB, even though PB impacts SF3b, which is dissociated from the
465 spliceosome (freeing the U2-branchpoint helix) by DHX16/Prp2 prior to the chemical steps of
466 splicing so that the active site of the spliceosome can form. We speculate that triggering the
467 use of different branchpoints via PB results in a dependency on weaker 3' splice sites, whose
468 docking into the catalytic core of the spliceosome requires stabilization by step 2 factors, a
469 model consistent with the cryoEM structure of the human post-catalytic P complex (Fica et al.,
470 2019).

471 Because the residues impacted by the PB-sensitive mutations are (by definition)
472 functional, one anticipates that they would not vary in the human population, given the essential
473 function of the spliceosome. Nonetheless, we asked this question by searching the ClinGen
474 database. Strikingly, residues altered in seven of the PB-sensitive mutants have been identified
475 in the human population (labelled as “non-disease-associated”) with four displaying the exact
476 same amino acid changes in the human population as in our PB-sensitive cells (Table S2),
477 suggesting that these variants very likely have a functional impact.

478

479 **Identification of SUGP1 G-patch mutations as PB-resistant**

480 Our studies identified two sgRNAs that target SUGP1 that produce PB-resistance. The
481 stronger of the two alleles produced by these guides, G603N, lies in a conserved domain of G-
482 patch proteins called the “brace loop” which is important for G-patch proteins to activate their
483 cognate DEAH-box helicase. The other change, E554K, lies just upstream in a region predicted
484 by AlphaFold2 to be helical. By performing proximity labelling, comparing wild-type versus
485 mutant proteins, we identified a single DEAH-box protein, DHX15/hPrp43 as being both
486 labelled by SUGP1-miniTurboID fusions and sensitive to a G-patch mutation obtained in our

487 screen. DHX15 has often been found in proteomic studies of early spliceosomes, but its
488 function at this stage remained relatively opaque. However, a recent study from Jurica and
489 colleagues has shown that depletion of DHX15 from HeLa cell extracts results in an increase
490 rather than a decrease in A complex formation (Maul-Newby et al., 2022). This result is
491 consistent with the observation that yeast Prp43 is the helicase that disassembles
492 spliceosomes (Martin et al., 2002; Tanaka et al., 2007). Taken together with our results and the
493 known association of SUGP1 with early spliceosomal complexes, we propose that SUGP1
494 recruits DHX15 to disassemble early spliceosomes, constituting an early discard step
495 analogous to late discard steps described by Staley and colleagues in yeast (Figure 7). In this
496 model, PB resistance results from mutation in the SUGP1 G-patch domain because this
497 increases A complex formation or residence time by inhibiting disassembly, thereby
498 counteracting the inhibitory activity of PB in reducing stable A complex formation.

499

500 **Relationship to oncogenic mutations in SUGP1 and SF3B1**

501 Manley and colleagues have proposed that cancer SF3B1 mutations act by limiting
502 association of SUGP1 with the spliceosome. This model, based on biochemistry, is supported
503 by genetic data that identified SUGP1 mutations in tumors that mimic the splicing phenotypes
504 of SF3B1 mutant tumors (Alsafadi et al., 2021). Indeed, many of the identified cancer mutations
505 map to the regions flanking the G-patch motif of SUGP1 (Figure S5F), which we show to
506 influence SUGP1-DHX15 interaction and splicing. It was proposed that the then-unknown
507 helicase that is recruited by SUGP1 might dissociate SF1 from the branchpoint, causing U2
508 snRNP to relocate to alternative branchpoints (Zhang et al., 2019). However, our discard model
509 proposes a different mechanism underpinning the effects of SUGP1 cancer mutations, namely
510 a defect in an early rejection step mediated by spliceosome disassembly (Figure 7). Such a
511 model would explain the activation of cryptic branchpoints as a defect in proofreading enabling
512 the production of oncogenic mRNAs via the activation of cryptic branchpoint/3' splice site
513 combinations as has been observed in SF3B1 and SUGP1 mutants (Liu et al., 2020; Zhang et
514 al., 2019). This model is also consistent with *in vitro* studies of DHX15 depletion described
515 above and the known activity of DHX15 in spliceosome disassembly.

516

517 **Mutagenesis of an essential machine in human cells in a haploid context**

518 While this work was underway, two laboratories recently independently reported the
519 deployment of base editor libraries in a variety of screens that involved phenotypic
520 characterization of single nucleotide variants and/or to probing of small molecule-protein
521 interactions (Cuella-Martin et al., 2021; Hanna et al., 2021) . These studies largely interrogated
522 individual proteins or part of a gene network and were mostly performed in diploid (or diploid-
523 like) cells. To enable large scale studies in a haploid context, we generated editing-competent
524 eHAP cells expressing the FLNS editor under conditions that maintained their haploid state. A
525 notable finding from this work is that editors produce unexpected mutations at low frequencies
526 which can produce phenotypes upon positive selection. For PHF5A, about half of the PB-
527 resistant mutants appeared to select for such mutations. While undesirable for the use of base
528 editing to generate specific programmed alleles, such unanticipated activities are useful for
529 mutagenesis studies. Given our experience with the spliceosome, the future is bright for using
530 base editing to interrogate essential cellular machines in human cells to produce new insights
531 into human cell biology and disease.

532

533 **Limitations of this study**

534 The editor we used in this study targets only a subset of residues in spliceosomal
535 proteins and is limited by base editor specificity and the occurrence of PAM sites. Thus, many
536 additional potential informative mutations may be isolatable with the advent of complementary
537 technologies that enable for efficient base editing at additional sites without causing unwanted
538 cellular toxicity. Our analysis of PB-hypersensitive sites requires further studies to understand
539 their mechanistic impact. Biochemical tests of the proofreading model will require its
540 reconstitution *in vitro* and, ultimately, structural analysis.

541

542

543 **Acknowledgements**

544 We dedicate this paper to the memory of Dr. Christine Guthrie. We thank all members of the
545 Madhani lab for scientific discussions and support. We thank Stefan Oberlin (UCSF) for advice
546 on bioinformatics analysis and CRISPR screens, Lukas E. Dow (Cornell) and David R. Liu
547 (Harvard) for advice on base editing, and Daniël van Leeuwen and Chris Richards for advice
548 regarding HAP1 cells. The authors thank Qing Feng and Chris Burge for communicating
549 unpublished results and for technical advice. Sequencing data was generated at the UCSF
550 CAT and through the kind use of their NextSeq System by Venice Servellita and Charles Chiu.
551 I.B. was supported by the Swiss National Science Foundation through an SNF Postdoctoral
552 Fellowship (191929 and 203008). Research in the Madhani lab is supported by R01 GM71801.
553 Mass Spectrometry was provided by the Mass Spectrometry Resource at UCSF (A.L.
554 Burlingame, Director) supported by the Dr. Miriam and Sheldon G. Adelson Medical Research
555 Foundation (AMRF) and the UCSF Program for Breakthrough Biomedical Research (PBBR).
556 Work in the Jonas lab was supported by the Swiss National Science Foundation (SNSF)
557 through the National Center for Excellence in Research “RNA & Disease” (grant number
558 205601) and through SNSF project grants (grant numbers 179498 and 207458).

559

560 **Author contributions**

561 Conceptualization and Methodology, I.B. and H.D.M.; Validation, Formal Analysis, and
562 Visualization, I.B.; Investigation, I.B., B.R., S.L., J.O-P., E.S., M.K.S, T. L., V.S.; Writing –
563 Original Draft, I.B., S.J. and H.D.M.; Writing – Review & Editing, all authors; Supervision, I.B.,
564 H.D.M., and S.J.; Funding Acquisition, I.B., H.D.M and S.J.

565

566 **MATERIALS AND METHODS**

567

568 **Lead contact**

569 Further information and request for resources and reagents should be directed to and will be
570 fulfilled by the Lead Contact, Hiten D. Madhani (hitenmadhani@gmail.com).

571

572 **Materials availability**

573 Plasmids generated in this study are available from the Lead Contact. Cell lines generated in
574 this study are not available as eHAP cells and any product derived thereof are protected under
575 an MTA upon purchase of the eHAP parental cell lines from Horizon (original vendor).

576

577 **Data and code availability**

578 The read counts for the CRISPR-Cas9 base editing screen is provided as Supplementary
579 Tables and the FASTQ files for screens, validation experiments are deposited on the Sequence
580 Read Archive. The accession number for the data reported is: XXXXX. RNA-seq data is
581 deposited on the Sequence Read Archive with the accession number: XXXX. The mass
582 spectrometry proteomics data have been deposited to the ProteomeXchange Consortium via
583 the PRIDE (Perez-Riverol et al., 2022) partner repository with the dataset identifier
584 PXD038067.

585

586 **METHOD DETAILS**

587

588 **Vectors**

589 Assembly of vectors (cloning and mutagenesis) was, if not otherwise indicated, performed
590 using NEBuilder® HiFi DNA Assembly (NEB #E2621).

591 *pLibrary (MP783)*: mU6 promoter expresses customizable guide RNA with a 20N barcode
592 sequence at the 3' end of the tracrRNA to facilitate identification of individual sgRNAs and
593 sample splitting into replicates (Boettcher et al., 2019). A core EF1 α promoter expresses
594 puromycin resistance and a T2A site provides BFP for easy titer determination of the lentiviral
595 library.

596 *pFNLS*: A core EF1 α promoter expresses 3xFLAG-tagged codon optimized FNLS base editor
597 and provides with a P2A site EGFP for identification of FNLS carrying cell lines. A PGK
598 promoter provides blasticidin resistance. This vector was modified from Addgene vector
599 #110869.

600 *pHA-SUGP1*: Point mutations and deletions were introduced with into p3xFLAG-CMV-14_3xHA
601 (Zhang et al., 2019).

602 *Vectors for BioID*: SUGP1 constructs were cloned from pHA-SUGP1 using primers (IB0156 5'-
603 atgacgtcccagactacgcagctagcAGTCTCAAGATGGACAACC-3'; IB0157 5'-
604 tgtttagcgttcagcagcgggatagatccgcctgaGTAGTAAGGCCGTCTGG-3') into pCDNA3_3xHA-
605 miniTurbo-NLS (Addgene #107172) digested with NheI-HF (NEB #R3131).

606 *Expression plasmids*: SUGP1 constructs were generated by PCR using a plasmid from the
607 human open reading frame library (hORFeome Version 5.1, ID: 53373) as template and gene-
608 specific primers. For protein expression in *E. coli*, the constructs were cloned into the NdeI-
609 XbaI sites of the plasmid pNEA-NpM, which is derived from the pET-MCN vector series that
610 harbors an N-terminal MBP-tag and a subsequent 3C protease site (Haffke et al., 2015).
611 Mutations in the SUGP1 constructs were introduced by 'round-the-horn' (RTH) mutagenesis
612 (Hemsley et al., 1989) using the respective primers (Table S3). The cloning and insect cell
613 expression of hsDHX15ΔN has been described previously (Studer et al., 2020b).

614

615 **Cell Culture**

616 All cell lines were maintained at 37 °C with 5% CO₂ and were regularly tested negative for
617 mycoplasma infection. Human embryonic kidney (HEK) 293T cells were grown in DMEM (with
618 4.5 g/L glucose, L-glutamine and sodium pyruvate; Corning #10-013-CV) supplemented with
619 10% FBS. Cells were passaged every 2-3 days.

620 Human eHAP cell lines and derivatives thereof were cultured in IMDM (with L-
621 glutamine, with HEPES; Cytiva #SH30228), supplemented with 10% FBS and 1:100
622 penicillin/streptomycin. eHAP cell lines were at all times maintained at sub-confluent conditions
623 and ploidy was regularly assessed with flow cytometry. When mentioned, doses of puromycin
624 were 4 µg/ml and blasticidin 10 µg/ml.

625 Flow cytometry data was analysed with FlowJo (v10.8.1).

626

627 **Cell viability assay**

628 96-well plates were seeded with 11000 cells per well earlier in the day and treatment was
629 started after allowing cells enough time to attach to the plate surface. A serial dilution of PB
630 was then used (starting at 100 nM and followed by 10 additional 2-fold dilution steps down to
631 0.25 nM or starting at 10 μ M, 1 μ M, 250 nM and followed by 7 additional 2-fold dilution steps
632 down to 0.98 nM). DMSO percentage was maintained throughout and a DMSO-only control
633 was included. 60 h post PB addition, CellTiter 96® AQueous One Solution Cell Proliferation
634 Assay reagent (Promega #G3582) was added and incubated for 4 h and read out according to
635 the manufacturer's instruction. Samples were measured in two technical replicates, whose
636 values were used as an average for three biological replicates. EC₅₀ curves were fit with
637 GraphPad PRISM.

638

639 **Spliceosome library design and production**

640 We compiled a list of all spliceosome components reproducibly detected through mass
641 spectrometry(MS), interaction studies, and/or purified and visualized in the spliceosome in
642 structural biology studies (Sales-Lee et al., 2021). This list encompasses 153 proteins (Table
643 S1). Guide sequences for targeting the spliceosome were designed using CHOPCHOP(Labun
644 et al., 2019) using [-Target \$GENE -J -BED -GenBank -G hg38 -filterGCmin 0 -filterGCmax 100
645 -consensusUnion -t CODING -n N -a 20 -T 1 -g 20 -M NGG]. We included all sgRNAs targeting
646 coding sequence across all exons in all isoforms, including 20 nucleotides into the introns and
647 UTR. Oligonucleotide pools were synthesised by CustomArray. Cloning sites were appended
648 with 5'- AGTATCCCTTGGAGAACCACCTTGTTGG-3' and 5'-
649 GTTTAAGAGCTATGCTGGAAACAGCATA-3'. The final oligonucleotide sequence was thus: 5'-
650 AGTATCCCTTGGAGAACCACCTTGTTGG [sgRNA, 20 nt]
651 GTTTAAGAGCTATGCTGGAAACAGCATA -3'.

652 Primers (forward: cttgAGAACCACCTTGTTG, reverse: GTTCCAGCATAGCTCTTAAAC)
653 were used to amplify the library pool (15x cycles). The resulting amplicons were PCR purified
654 (QIAGEN #28104) and cloned into the library vector [digested with AarI (ThermoFisher
655 #ER1582)] via Gibson assembly (NEBuilder® HiFi DNA Assembly). The ligation product was
656 buffer exchanged (BioRad #732-622) ethanol precipitated and electroporated into MegaX

657 DH10B T1^R Electrocomp™ Cells (ThermoFisher #C640003). The plasmid DNA was sequenced
658 to confirm library and barcode representation and distribution.

659

660 **Spliceosome library annotation**

661 CRISPR-Cas9 base editing outcomes were predicted according to the following rationale. We
662 assumed that if editing occurs for a given sgRNA, all cytosines within the editing window
663 (position 3-8) will be mutated to thymine, with the exception of Cs at positions 3, 4, 6, 7, and 8 if
664 they are preceded by a G(Kluesner et al., 2018). This was used to classify sgRNAs into non-
665 editing (= sgRNAs containing no C within editing window), non-editing_GC (= sgRNAs
666 containing C's in GC context unfavorable to editing, not at position 5 within sgRNA), and editing
667 sgRNAs. Editing sgRNAs were further classified by MNV (multiple nucleotide variant) prediction
668 using VEP (McLaren et al., 2016) . For each MNV, where available only the outcome for MANE
669 (Matched Annotation between NCBI and EBI) transcript was considered. In a next step,
670 consequences were binned into categories and consequence severity was given in this order:
671 CDS_missense > stop_gained > start_lost > SS_acceptor, SS_donor, SS_region, CDS_silent >
672 3'UTR > 5'UTR. It should be noted, that VEP considers a splice site region variant a sequence
673 variant with a mutation within 1-3 bases of the exon or 3-8 bases of the intron.

674

675 **Virus production and MOI determination**

676 For lentivirus generation and packaging, media for HEK293T cells was supplemented with non-
677 essential amino acids (Gibco #25300054). Cells were seeded 24 h before transfection with
678 jetPRIME reagent (Polyplus #114-15) at a 2.5 µl to 1 µg DNA ratio. Media was changed 6 h
679 post transfection and fresh media was supplemented with ViralBoost Reagent (Alstem
680 #VC100).

681 The packaging mix consisting of psPAX2 (Addgene #12260) and pMD2.G (Addgene #12259)
682 was prepared at a molar ratio of 1:1. The following reagents were adapted according to scale of
683 lentivirus production:

684 24-well plate: 2e5 cells seeded, 450 ng target DNA + 450 ng packaging mix per well.

685 6-well plate: 7.5e5 cells seeded, 1 µg target DNA + 1 µg packaging mix per well.

686 10 cm plate: 5.2e6 cells seeded, 5.5 µg target DNA + 4.5 µg packaging mix per dish.
687 Virus was generally concentrated using Lentivirus Precipitation Solution (Alstem #VC100).
688 Virus was titered by seeding 2e5 eHAP FNLS cells in 1 ml media per 6-well plate and
689 immediately adding sequentially diluted virus amounts. 48 h post-transduction the number of
690 BFP positive cells was assessed by flow cytometry. A viral dose resulting in 30-40%
691 transduction efficiency, corresponding in an MOI of ~0.3, was used for all subsequent
692 experiments.

693

694 **Generation of eHAP FNLS cell line**

695 Lentivirus was generated with pFNLS and transduced on eHAP cells. Cell lines were selected
696 with blasticidin four days post-transduction for one week and then single cell sorted to obtain
697 monoclonal cell lines. Editing rate of a cell line was assessed by transduction with control
698 sgRNAs (EMX1, HEK2, HEK3, HEK4) and evaluation using sanger sequencing of the editing
699 window and EditR (Kluesner et al., 2018). Clonal cell lines showing high rates of base editing
700 were treated with 10 µM 10-deacetylbaicatin-III (Selleckchem #S2409) for 10-15 days with
701 ploidy assessed every second day. Treatment was stopped as soon as an exclusively haploid
702 cell population was achieved. Editing rate was re-assessed and no changes were observed.

703

704 **Generation of eHAP FNLS mutant cell lines**

705 eHAP FNLS cells were transduced with lentivirus carrying a single sgRNA at an MOI of 0.3.
706 After 2 days sgRNA carrying cells were selected using puromycin for four days. Cells were
707 given two days to recover from selection pressure and then seeded as single cells by limited
708 dilution. The SF3B1 T1080I and PHF5A 2xTL mutations were obtained by first treating cells for
709 2 weeks with 2 nM PB to enrich for the mutations.

710 Single cell colonies were maintained and expanded while assessing ploidy and
711 genotyping the clones. Genotyping was performed by using QuickExtract™ DNA Extraction
712 Solution (Lucigen #QE09050) on a fraction of a clone. The region of interest was amplified
713 using custom primers and sanger sequenced. After expansion of the single cell, ploidy was
714 again assessed before freezing the cell line for long term storage.

715

716 **Ploidy assessment for eHAP cell lines**

717 After harvesting, cells are washed with flow cytometry buffer (1x DPBS with 2% FBS, 4 mM
718 EDTA pH 8) and stained on ice with 0.1% sodium citrate, 0.1% Triton X-100, 50 µg/ml
719 propidium iodide for 5 min and immediately assessed by flow cytometry(Beigl et al., 2020).

720

721 **Spliceosome-wide CRISPR-Cas9 base editing screen**

722 The screen was performed at 500x sgRNA representation for entire duration. 66 million eHAP
723 FNLS cells were infected with the lentiviral spliceosome library (marked with BFP) at an MOI of
724 ~0.3, such that every sgRNA was represented in approximately 500 cells. Puromycin selection
725 was started at 48 h post transduction. At six days post-transduction, cells were assessed by
726 flow cytometry to only contain sgRNA carrying cells (BFP-positive cells >95%). Cells were then
727 split into treatment arms (DMSO vs. 2 nM PB; with identical DMSO concentration in both
728 treatment arms). Cells were propagated and treatment was renewed every second day.

729 At screen end point cells were harvested and gDNA was extracted with QIAamp DNA
730 Blood Maxi Kit (Qiagen #51194). Genome weight was estimated based on measured ploidy of
731 cells. The sequencing library was prepared using NEBnext® Ultra II Q5 Master Mix (NEB
732 #M0544) and custom primers (forward: IB0096-IB0104; reverse IB0106-IB0121) to have a
733 balanced read sample. A barcode in the reverse primer was used for identification of the
734 sequencing libraries. Libraries were gel-purified and cleaned up. Libraries were balanced and
735 quality was assessed with Bioanalyzer High Sensitivity DNA Kit, Agilent #5067-4626).

736

737 **Validation experiments**

738 For validation experiment, 45 individual sgRNAs targeting the spliceosome were cloned into
739 pLibrary containing EF1α-puro-T2A-BFP and made into lentivirus as described above. sgRNAs
740 were selected for significant enrichment or depletion ($LFC > |2|$, $padj < 0.05$). Moreover, we
741 took statistically not significantly enriched/depleted sgRNAs if they were strongly enriched (LFC
742 > 2.75) or depleted ($LFC < -3.5$). The threshold was set to approximately mimic the lowest level
743 of enrichment or depletion observed, respectively, for the statistically significant sgRNA. All

744 depleted sgRNAs further had to fulfil $LFC > -1$ for a comparison of t14 vs. t0 in the control
745 condition. In addition, three non-targeting sgRNAs were cloned into pLibrary containing EF1 α -
746 puro-T2A-mCherry and into pLibrary EF1 α -puro-T2A-BFP (see Table S3 for full list and
747 primers). Lentivirus was generated and titered as described above. 2e5 eHAP FNLS cells were
748 transduced with individual sgRNA lentivirus in 6-well plates. Puromycin selection was started
749 36 h post-transduction and continued for four days. Care was taken to maintain all cells haploid
750 (as diploid cells grow faster) and ploidy was checked with flowcytometry as described above.
751 On day 6 (= t0) cells were grouped according to their growth density on plate and a
752 representative sample was counted. An estimated 5500 cells per spliceosome sgRNA or non-
753 targeting sgRNA carrying cells were each mixed with 5500 cells carrying sgNTC_400.
754 Treatment was started on the next day (DMSO vs. 2 nM PB) and cells were passaged as
755 needed with treatment renewed every second day. The ratio of BFP:mCherry was assessed at
756 t0, t4, t8 and t15.

757

758 **Library and sequencing for base editing window**

759 Lentivirus from validation experiment was used to transduce 2e5 eHAP FNLS cells at MOI 0.3
760 in a 6-well dish. After puromycin selection on day 6 (= t0), 2x 11000 cells were seeded in 96-
761 well plates and split into treatment arms the next day (DMSO vs. 2 nM PB). Cells were
762 propagated and harvested at t8 and t14 for gDNA extraction. Genomic DNA was extracted
763 using QuickExtract™ DNA Extraction Solution (Lucigen #QE09050) and 1 μ l (qsp. >200 cells)
764 and was used for target site amplification using a 2-step PCR. In addition, each reaction
765 contained 10 μ l NEBnext Ultra II Q5 master mix as well as 1 μ M of each forward and reverse
766 primer. Primer pairs for PCR 1 were selected such that forward annealing primer is not closer
767 than 7 nt to editing window position 1 but still allowing that 75 sequencing cycles will read the
768 sequence. Primers were verified to anneal to a single position within the genome using BLAT
769 (Kent, 2002) and tested before use. Primers for PCR 1 (12 cycles) were flanked for the forward
770 primer by: 5'-ACACTCTTTCCCTACACGACGCTCTTCCGATCT-[target specific sequence]-3'
771 and for the reverse primer by 5'-GTGACTGGAGTTCAGACGTGTGCTCTTCCGATCT-[target
772 specific sequence]-3'. 1.5 μ l of PCR 1 were used as template for PCR 2 (14 cycles) and used

773 forward primers 5'-AATGATACGGCGACCACCGAGATCTACAC-NNNNNNNN-
774 ACACTCTTTCCTACACGAC-3' (compatible to Illumina i5) and reverse primers 5'-
775 CAAGCAGAAGACGGCATAACGAGAT- NNNNNNNN- GTGACTGGAGTTCAGACGTG-3'
776 (compatible to Illumina i7), with both containing 8N barcodes for multiplexing.
777 Primers were removed after the second PCR step with AMPure XP Reagent (Beckman
778 #A63882). Library was quantified (QuantiFluor® dsDNA System; Promega #E2670) before
779 being pooled (10 fmol per sample) for each time point & condition, run on 8% TBE-PAGE gel,
780 then size selected for a range of 250-500 bp. Pooled libraries were then run on Bioanalyzer
781 High Sensitivity DNA Kit, Agilent #5067-4626) before final pooling and subsequent run on a
782 MiniSeq Sequencing System using the Miniseq High Output Kit (75 cycles) (Illumina #FC-420-
783 1001) with a 10% of phiX spike-in.

784

785 **RNA-seq**

786 eHAP FNLS and mutant cells were treated for 3 h with DMSO or 2 nM PB before cells were
787 harvested. This was done for three replicates of an eHAP FNLS cell line transduced with a non-
788 targeting sgRNA. Total RNA was extracted using the RNAqueous™-96 Total RNA Isolation Kit
789 (ThermoFisher #AM1920) according to the manufacturer's protocol. Poly(A)-enriched RNA was
790 obtained with the poly(A) RNA Selection Kit V1.5 (Lexogen #157.96) and RNA-seq libraries
791 were generated using the CORALL Total RNA-Seq Library Prep Kit (Lexogen #117.96). The
792 libraries were then sequenced using paired-end 150 bp reads with 60 million reads per sample
793 on Nova Seq (S4).

794

795 **RNA extraction and RT-PCR**

796 RNA was extracted from cells using the RNeasy Plus Mini Kit (Qiagen #74134) according to
797 the manufacturer's protocol. Reverse transcription using either SuperScript III (Invitrogen
798 #18080093) or SuperScript IV (Invitrogen #18090050) was performed according to the
799 manufacturer's protocol using a mix of random hexamer primers and oligo(dT) using an input of
800 500 ng total RNA for a 10 µl reaction. PCR was performed with junction specific primers (Table
801 S3) using 2% of the cDNA as an input for a 25 µl PCR reaction. PAGE was visualized using

802 SYBR Gold (Invitrogen #S11494) and intensity of PCR products were quantified using ImageJ
803 (NIH).

804

805 **BiOD sample preparation for MS**

806 6 million HEK293T cells were seeded on 150 mm plates and transfected 24 hours later with 15
807 µg plasmid using jetPRIME reagent (at a 1:2.5 ratio for µg DNA:µl jetPRIME reagent; Polyplus
808 #114-15). Transfection was performed in four independent biological replicates. Media was
809 replaced with fresh culture media 5-6 h post transfection. At 24 h post transfection, a biotin
810 pulse of 2 min biotin (culture media supplemented with 200 µM biotin) was used for proximity
811 labelling. Cells were then immediately placed on ice and washed five times with ice cold DPBS
812 (Corning #21-031-CV) before collection by gentle repeat pipetting. Cell pellets were lysed in
813 1500 µl ice cold RIPA buffer (50 mM Tris-Cl pH 7.4, 150 mM NaCl, 1% NP40, 0.5% Na-
814 deoxycholate, 0.1% SDS, 1 mM EDTA, Roche cOmplete and 1 mM PMSF). Cell lysates were
815 clarified by centrifugation (13000 x g at 4°C for 10 min) before quantification with BCA protein
816 assay (Thermo #23227). 2.5 mg protein in 1500 µl RIPA buffer were added to 250 µl MyOne
817 Streptavidin T1 Dynabeads (Invitrogen #65602), prewashed twice with 1 ml RIPA buffer.
818 Protein and beads were incubated for 30 min at 4 °C with rotation to capture biotinylated
819 proteins. Beads were then pelleted on magnet and washed twice with RIPA buffer (1 ml for 2
820 min at RT), washed once with 1 M KCL (1 ml for 2 min at RT), washed once with freshly made
821 0.1 M Na₂CO₃ (1 ml for 10 s), washed once with freshly made 2 M urea in 10 mM Tris.Cl pH 8
822 (1 ml for 10 s), before washing twice more with RIPA buffer (1 ml per wash, 2 min at RT).
823 Beads were resuspended in 200 µl RIPA buffer before transfer to a new low binding tube.
824 Beads were then washed in 200 µl 50 mM Tris.Cl pH 7.5, twice in 200 µl 2 M urea in 10 mM
825 Tris.Cl pH 7.5, and twice in 200 µl H₂O.

826 Bead pellet was frozen for handover to MS facility.

827

828 **On beads Digestion and TMT labelling**

829 Sample-incubated streptavidin magnetic beads were resuspended in 9 µl 5 mM Tris(2-
830 carboxyethyl)phosphine 20mM triethylammonium bicarbonate and incubated for 30 min at

831 room temperature. After this, iodoacetamide was added to a final concentration of 7.5 mM, and
832 samples incubated for 30 additional minutes. 1 µg of LysC (Fujifilm Wako Pure Chemical
833 Corporation) was added to each sample and incubated at 37 °C overnight. Then 1 µg
834 sequencing grade trypsin (Promega) was added to each sample and incubated at 37 °C
835 overnight. Supernatants of the beads were recovered, and beads digested again using 0.5 µg
836 trypsin in 100mM NH₄HCO₃ for 2 h. Peptides from both consecutive digestions were combined
837 and recovered by solid phase extraction using C18 ZipTips (Millipore), eluted in 15 µl 50%
838 acetonitrile 0.1% formic acid, and evaporated. Samples were then resuspended in 8 µl 0.1 M
839 triethylammonium bicarbonate pH 8.0. Dried samples were labelled according to TMTProTM-16
840 label plex kit instructions (ThermoFisher Scientific). Briefly, TMT reagents were dissolved in
841 acetonitrile at 12.5 µg/µl, and 4 µl of these stocks added to the samples. After incubation for 1 h
842 at room temperature samples were quenched with 1ul 5% hydroxylamine, and all 16 samples
843 were combined, partially evaporated, and desalted using a C18 ZipTip as described before.
844 The eluate was dried in preparation for LC-MSMS analysis.

845

846 **Mass Spectrometry Analysis**

847 Samples coming from RP fractionation were run onto a 2 µm, 75µm ID x 50 cm PepMap RSLC
848 C18 EasySpray column (Thermo Scientific). 3-hour MeCN gradients (2–30% in 0.1% formic
849 acid) were used to separate peptides, at a flow rate of 300 nl/min, for analysis in a Orbitrap
850 Lumos Fusion (Thermo Scientific) in positive ion mode. MS spectra were acquired between
851 375 and 1500 m/z with a resolution of 120000. For each MS spectrum, multiply charged ions
852 over the selected threshold (2E4) were selected for MSMS in cycles of 3 seconds with an
853 isolation window of 0.7 m/z. Precursor ions were fragmented by HCD using stepped relative
854 collision energies of 30, 35 and 40 to ensure efficient generation of sequence ions as well as
855 TMT reporter ions. MSMS spectra were acquired in centroid mode with resolution 60000 from
856 m/z=110. A dynamic exclusion window was applied which prevented the same m/z (mass
857 tolerance 30 ppm) from being selected for 30s after its acquisition.

858

859 **Immunoblotting**

860 Cell lysates were mixed with NuPAGE LDS Sample Buffer (Invitrogen #NP00007), heated for 5
861 min at 95 °C, separated on SDS-PAGE gels and transferred to nitrocellulose membranes. Blots
862 were either incubated for 1 h at RT or overnight at 4 °C with the following primary antibodies in
863 TBS-T with 5% milk: α -HA (Cell Signalling Technology, #3724) at 1:5000; α -GAPDH-HRP
864 (Proteintech, #HRP-60004) at 1:10,000. HRP-conjugated streptavidin (Invitrogen, #S911)
865 reconstituted at 1 mg/ml was used at 0.3 μ g/ml in 3% (w/v) BSA in 1x TBST and blots were
866 only incubated for 30 min in its presence.

867

868 **Protein expression and purification**

869 For pulldown and RNA binding assays, MBP-*hsSUGP1* variants were expressed *E. coli* BL21
870 Star (DE3) (Invitrogen). Cells were grown at 37°C in LB medium until an OD₆₀₀ of 0.6 was
871 reached. Protein expression was induced with 2 mM isopropyl- β -D-thiogalactopyranoside
872 (IPTG) and maintained at 37°C for 3 h. Expression cultures were harvested by centrifugation
873 and cell pellets were resuspended in lysis buffer (50 mM Hepes, pH 7.5, 200 mM NaCl, 2 mM
874 dithiothreitol [DTT]) supplemented with cOmplete EDTA-free protease inhibitor mixture
875 (Roche), 1 mg/mL lysozyme (Sigma), and 5 μ g/mL DNaseI (Roche). For cell lysis, the
876 suspension was passed through a LM10 Microfluidizer. Subsequently, the lysate was
877 cleared by centrifugation at 3200 g for 10 min and filtered (0.45 μ m). Lysates were incubated
878 with preequilibrated amylose beads (New England BioLabs) for 1 h at 4°C. Beads were washed
879 with lysis buffer and bound proteins were eluted with lysis buffer containing 25 mM maltose.
880 The eluates were concentrated, loaded onto a gel-filtration column (Superdex 200, GE
881 Healthcare) and eluted in size-exclusion buffer (10 mM Hepes, pH 7.5, 200 mM NaCl, 2 mM
882 DTT). The MBP-*hsSUGP1* variants were either directly used in biochemical assays or flash-
883 frozen in liquid nitrogen and stored at -80°C.

884 For the ATPase assay, MBP-*hsSUGP1* variants were subjected to additional washes while
885 bound to the amylose beads during the first purification step to remove ATPase contamination.
886 Bound proteins were incubated with lysis buffer supplemented with 2 mM ATP and 2 mM
887 MgCl₂ for 10 min at 4°C and washed with lysis buffer containing 1 M NaCl. After the high-salt
888 wash, beads were equilibrated again in lysis buffer before elution as described above.

889

890 **Protein binding assays**

891 For interaction studies, purified His₁₀-*hsDHX15ΔN* and MBP-*hsSUGP1* variants were mixed in
892 equimolar amounts in pulldown buffer (50 mM Hepes, pH 7.5, 200 mM NaCl, 2 mM DTT). His₆-
893 MBP was used as a negative control. Proteins were incubated with 50 μl of amylose beads
894 (50% slurry in pulldown buffer) for 1 h at 4°C on a rotator. The beads were washed three times
895 in pulldown buffer. Bound proteins were eluted with pulldown buffer containing 25 mM maltose.
896 Proteins of input and eluate samples were separated by sodium dodecyl sulfate
897 (SDS)/polyacrylamide gel electrophoresis (PAGE) and were visualized by Coomassie staining.

898

899 **RNA Binding Assays**

900 RNA binding affinities of His₁₀-*hsDHX15ΔN* in complex with MBP-*hsSUGP1* variants were
901 determined by measuring changes of fluorescence polarization (FP) in dependence of protein
902 concentration, as previously described (Studer et al., 2020b). Experiments were performed in
903 binding buffer (20 mM Hepes (pH 7.5), 150 mM NaCl, 5% glycerol and 2 mM MgCl₂) with
904 10 nM 5'-6-fluorescein amidites (FAM)-labelled U₁₂ RNA (Microsynth) and protein
905 concentrations ranging from 1 nM to 32 μM. FP was determined using a CLARIOstar
906 microplate reader (BMG Labtech) by excitation at 482 nm and detection at 530 nm wavelength.
907 All samples were measured five times and all samples were prepared in triplicates. After
908 baseline subtraction, the obtained FP values were normalized to 1 and fitted according to Rossi
909 *et al.* using GraphPrad Prism (Rossi and Taylor, 2011).

910

911 **ATPase assays**

912 Activity of *hsDHX15* and its interactor *hsSUGP1* were monitored using an NADH-coupled
913 ATPase assay. For all measurements of ATPase activity, 1.8 μM His₁₀-*hsDHX15ΔN* and
914 1.8 μM MBP-*hsSUGP1* variants (G-patch (548-611)) were mixed in ATPase buffer containing
915 50 mM Hepes pH 7.5, 50 mM KAc, 5 mM MgAc₂, 2 mM DTT, 0.5 mM nicotinamide adenine
916 dinucleotide, 1 mM phosphoenolpyruvate, 12 U of pyruvate kinase, and 18 U of lactate
917 dehydrogenase. All measurements were carried out in half area 96-well plates (Greiner). After

918 equilibration for 10 min at 37°C, reactions were started by adding 250 μM ATP (pH 7.5).
919 Absorption at 340 nm was measured over a time course of 40 min at 37°C with one
920 measurement per minute using a CLARIOstar microplate reader. Absorption change in the
921 absence of ATP was measured for baseline correction. Absorption values were adjusted to a
922 path length of 1 cm. Absorption change over time was determined by linear regression and
923 converted to concentration change over time with an extinction coefficient at 340 nm of 6,220
924 M⁻¹cm⁻¹ using Beer–Lambert's law. Initial velocities were derived from concentration change
925 over time using a total enzyme concentration of 1.8 μM. All measurements were prepared in
926 triplicates. Absence of ATPase contaminations from *hsSUGP1* preparations was confirmed by
927 measuring ATPase activity in the absence of *hsDHX15ΔN*.

928

929 **DATA ANALYSIS**

930

931 **Screen analysis**

932 The sequencing data was demultiplexed to obtain individual samples for timepoints and
933 trimmed (BBMap BBDuk v.38.94). Reads were counted by alignment to a reference file of all
934 sgRNAs present in the pool. In the next step, each barcode was randomly assigned to either of
935 two replicates. 32 sgRNA targeted 2 loci and their reads were duplicated and assigned to both
936 targets. Log₂-fold changes between samples were calculated using DESeq, filtering out reads
937 with on average less than 50 reads across all samples(Love et al., 2014).

938

939 **Identification of causative mutations**

940 Editing at the base editing window was quantified using CRISPResso2 v.2.1 (Pinello et al.,
941 2016), run with the following parameters: [--exclude_bp_from_left 18 --exclude_bp_from_right 0
942 --quantification_window_center -12 --quantification_window_size 15 --
943 min_average_read_quality 30 --default_min_aln_score 60 --plot_window_size 20 --
944 base_editor_output --output_folder 20210531_pos -p 12]. For analysis we used the
945 “Alleles_frequency_table_around_[sgRNA].txt” output files or in the single case where editing

946 occurred far outside the editing window “Alleles_frequency_table.txt” was used for information
947 extraction.

948 Samples were processed to only consider those with 100 or more reads per condition
949 across all conditions. In addition, all alleles with <1% in all conditions were removed before re-
950 calculating percent distribution of alleles. Alleles were translated and grouped by protein
951 sequence outcome and for each percent distribution was summed. Log₂-fold change was
952 calculated for samples

953 *Validation of PB sensitive samples:* For samples depleted in the screen, only sequencing data
954 corresponding to t₀ were considered. Mutational outcome was noted for any event with >5%
955 frequency.

956 *Validation of PB resistant samples:* All timepoints and treatment conditions were considered for
957 the analysis.

958

959 **Splicing analysis**

960 The RNA-seq data was demultiplexed, trimmed (BBMap BBDuk v.38.94), and then
961 mapped using STAR 2.7.9 (Dobin et al., 2013) [--alignSJoverhangMin 8 --
962 alignSJDBoverhangMin 1 --outFilterMismatchNmax 999 --alignIntronMin 20 --alignIntronMax
963 1000000 --alignMatesGapMax 1000000 --peOverlapNbasesMin 10 --peOverlapMMp 0.2] and
964 SAMtools (v1.10) for conversion to sorted bam files. Reads were then deduplicated using the
965 UMIs from the Lexogen CORALL workflow to prevent removal of natural duplicates. On
966 average, 85% of the reads could be mapped and quality assessment using the RSeQC
967 package (Wang et al., 2012) showed neither a bias in read distribution nor gene body
968 coverage. Differential expression of genes was assessed using RSubreads (Liao et al., 2019)
969 for counting and DESeq2 (Love et al., 2014). To analyze splicing at the exon level only
970 junctions with more than 10 junction reads were considered. We used rMATS-turbo (Shen et
971 al., 2014a) (hereafter, rMATS) for quantification. For all analysis performed with rMATS only
972 splicing junctions with FDR < 0.01 were considered. Alternatively, we also used MAJIQ(v2.4)
973 (Mehmood et al., 2020) with |dPSI| ≥10 and Confidence Threshold > 90%. For analysis of

974 intron and exon features we used the software matt (Gohr and Irimia, 2019). When preparing
975 figures with IGV, junction reads with low numbers were removed for clarity

976

977 **Peptide and protein identification and TMT quantitation.**

978 Peak lists were generated using PAVA in-house software (Guan et al., 2022). All generated
979 peak lists were searched against the human subset of the SwissProt database
980 (SwissProt.2019.07.31), using Protein Prospector (Clauser et al., 1999) with the following
981 parameters: Enzyme specificity was set as Trypsin, and up to 2 missed cleavages per peptide
982 were allowed. Carbamidomethylation of cysteine residues, and TMTPro16plex labelling of
983 lysine residues and N-terminus of the protein were allowed as fixed modifications. N-acetylation
984 of the N-terminus of the protein, loss of protein N-terminal methionine, pyroglutamate formation
985 from of peptide N-terminal glutamines, and oxidation of methionine were allowed as variable
986 modifications. Mass tolerance was 10 ppm in MS and 30 ppm in MS/MS. The false positive rate
987 was estimated by searching the data using a concatenated database which contains the
988 original SwissProt database, as well as a version of each original entry where the sequence
989 has been randomized. A 1% FDR was permitted at the protein and peptide level. For
990 quantitation only unique peptides were considered; peptides common to several proteins were
991 not used for quantitative analysis. Relative quantization of peptide abundance was performed
992 via calculation of the intensity of reporter ions corresponding to the different TMT labels,
993 present in MS/MS spectra. Intensities were determined by Protein Prospector. Summed
994 intensity per sample on each TMT channel for all identified carboxylases were used to
995 normalize individual intensity values. Relative abundances were calculated as ratios vs the
996 average intensity levels in the 4 channels corresponding to control samples. For total protein
997 relative levels, peptide ratios were aggregated to the protein levels using median values of the
998 log₂ ratios.

999

1000 **Software for data visualization and statistical analyses**

1001 For visualisation of cryo-EM and crystal structures we used PyMOL (v2.3.5), for visual
1002 presentation we used R ggplot2 (v3.3.6) with MetBrewer (v0.2.0.) and ggVennDiagram (v1.2.0)

1003 or pheatmap (v1.0.12), and GraphPad Prism (v8), and the Integrative Genomics Viewer (IGV)
1004 (v2.12.2). Schematics were created with Adobe Illustrator 2023.
1005 All statistical analyses were performed in R (v4.1.2) using base R or package multcomp.
1006 Statistical significance of one-way ANOVA or t-test is indicated by asterisks (* $p < 0.05$, ** $p <$
1007 0.01 , *** $p < 0.001$), unless otherwise indicated.

1008

1009

1010 **FIGURE LEGENDS**

1011

1012 Figure 1. CRISPR-Cas9 base editing screen targeting the spliceosome reveals several mutants
1013 sensitive or resistant to the small molecule spliceosome inhibitor pladienolide B.

1014 (A) Schematic of intron sequences required for splicing and the spliceosome cycle across the
1015 major assembly stages. Depicted are involved snRNPs, important subcomplexes, proteins and
1016 helicases. Point of action of the small molecule spliceosome inhibitor pladienolide B (PB) is
1017 indicated.

1018 (B) List of spliceosomal genes targeted by the sgRNA library.

1019 (C) Schematic of tiling sgRNA library. Every available PAM sequence (denoted in dark blue) on
1020 both strands of the genome is targeted across all coding exons. CRISPR-Cas9 cytosine base
1021 editor is targeted to the genomic DNA through the sgRNA to promote C > T editing within each
1022 sgRNA's editing window (marked in pink). This results in a theoretical cumulative range
1023 targetable by base editing.

1024 (D) eHAP FNLS cell line can be maintained in a haploid state. Shown is the flow cytometry
1025 analysis of DNA content via propidium iodide staining at various days corresponding to the
1026 control arm of our CRISPR-Cas9 base editing screen.

1027 (E) Schematic of the pooled screen. After transduction cells are given six days for
1028 mutagenesis by the CRISPR-Cas9 base editor. Cells are then split into treatment arms (DMSO
1029 vs. 2 nM PB) and collected after 14 days of culturing for DNA extraction and deep sequencing.

1030 (F) Results of screen. MA-plot comparing day 14 of cells grown in presence or absence of 2 nM
1031 PB. For orientation lines indicate a \log_2 -fold enrichment or depletion of two. sgRNA with strong

1032 sensitivity to PB are emphasized in green (dark green: $p\text{-adj} < 0.05$, light green: $p\text{-adj} \geq 0.05$
1033 but highly depleted). sgRNAs resulting in PB resistance are colored by protein target. For
1034 clarity, only data points for sgRNAs that passed the confirmation assay are shown. Dashed
1035 line: sgRNA targeting the same position and predicted to result in identical mutational outcome.
1036 Dark green: statistically significantly depleted sgRNAs. Light green: strongly depleted sgRNAs.

1037

1038 Figure 2. Pladienolide B sensitive mutations occur predominantly in early spliceosomal
1039 complexes.

1040 (A) Schematic of the arrayed confirmation assay. Individual sgRNA are transduced, marked
1041 with BFP, and cells are mixed 1:1 with non-targeting sgRNA carrying cells, marked by mCherry.
1042 Cell populations are left to compete during 15 days of growth in either DMSO or 2 nM PB
1043 treatment. The ratio of BFP:mCherry is measured with flow cytometry.

1044 (B) Individual sgRNAs and their performance in the confirmation assay. sgRNAs are grouped
1045 by category they were found in in the primary screen. Measurements are from three
1046 independent transductions ($n=3$). *, **, ***: Student's t-Test (paired) P value < 0.05 , 0.01 , 0.001 ,
1047 respectively.

1048 (C) Assignment of proteins targeted by sgRNAs conferring hypersensitivity to PB to the
1049 spliceosome cycle. Factors are indicated at their respective first step of action. *Saccharomyces*
1050 *cerevisiae* (*Sc.*) names are given where applicable. If multiple sgRNAs are found for a protein,
1051 this is indicated with a number in parenthesis.

1052 (D) Close-up of location of PB-sensitive SF3A1 G159K mutation plotted on the structure of
1053 SF3b bound to PB. It lies at the interface of SF3B3 (green), SF3B1 (violet) and PHF5A (teal).
1054 (PDB: 6EN4)

1055 (E) Comparison of SF3B3, SF3B1 and PHF5A in the structure of SF3b bound to PB and the A-
1056 like complex. SF3B1 undergoes a large conformational rearrangement from the open to the
1057 half-closed state. For easier tracking of the conformational change, HEAT repeat 1 (HEAT1) is
1058 indicated. Locations of PB-sensitive mutations are marked in magenta. (PDB: 6EN4, 7Q4O)

1059

1060 Figure 3. Novel resistance mutations in SF3B.

1061 (A) Schematic of workflow to identify phenotypic mutations. *Left*: Cells are transduced with
1062 single sgRNA in an arrayed format. After six days (t₀) treatment is initiated and a cell sample is
1063 harvested at t₀ as well as t₈ and t₁₅ for genomic DNA (gDNA) extraction. *Middle*: Locus-
1064 specific primers are used to amplify the editing window and its flanking sequence of the gDNA.
1065 The amplicons are then deep sequenced to identify mutations. *Right*: Mutational outcomes are
1066 translated and the resulting protein sequences are aggregated as multiple DNA sequences
1067 may result in the same protein sequence. Prevalence of each protein sequence is calculated
1068 for each time point and treatment condition. Where applicable, log₂-fold changes are calculated
1069 between two samples. Finally, time points and treatments can be compared across samples for
1070 both prevalence and/or log₂-fold change to the wild type (wt). Inferred phenotypic mutations
1071 (most prevalent at t₁₅ +PB) are indicated by a green background.

1072 (B) Editing outcome for sgSF3B1_166: In the absence of PB across t₀, t₈ and t₁₅ the wt is the
1073 only occurring protein (100% prevalence). Upon PB treatment, SF3B1 T1080I rapidly enriches
1074 (t₁₅ = 100% prevalence). This striking behaviour is emphasised by the log₂-fold change for this
1075 sgRNA.

1076 (C) Editing outcome for sgPHF5A_6: In the absence of PB some mutations occur within the
1077 editing window around R44. PB treatment enriches for a rare 6 nucleotide insertion occurring
1078 from the nicking action of the nCas9, which is part of FNLS. The resulting mutation is PHF5A
1079 TL insertion between C40 and T41 in PHF5A resulting in a tandem TLTL sequence.

1080 (D) Location of SF3B1 T1080I resistance mutation: SF3B1 HEAT repeats 15,16, and 17 (H15,
1081 H16, H17), which form part of the PB binding pocket (PB illustrated in yellow). H15 and H16
1082 form a hinge within SF3B1 which undergoes a closing motion upon BP-A binding. T1080
1083 (magenta) is located on the back of H15 facing away from PB and towards H14 (not shown).
1084 Known resistance mutations at K1071, R1074, V1078 are shown with side chains indicated.
1085 (PDB: 6EN4)

1086 (E) Location of PHF5A resistance mutations: All mutations are indicated (magenta) and occur
1087 on the face of PHF5A involved in PB binding. Y36C is also indicated – the only previously
1088 known PB resistance mutation in PHF5A. (PDB: 6EN4)

1089 (F) Illustration of SF3B1 and PHF5A resistance mutations in context of U2snRNP (A-like
1090 conformation). Mutations (magenta, circled) occur in vicinity to the branch helix and
1091 branchpoint adenosine. (PDB: 7Q4O)

1092 (G) Sixty-hour cell proliferation profiling (CellTiter-AQueous cellular viability and cytotoxicity
1093 assay) of control eHAP FNLS cell line expressing non-targeting sgRNA and monoclonal cell
1094 lines carrying either SF3B1 T1080I or PHF5A 2xTL mutation to PB. Error bars indicate s.d. n =
1095 3 (average of two technical replicates for independent clonal cell lines).

1096

1097

1098 Figure 4. Novel resistance mutations in SUGP1.

1099 (A) Schematic of SUGP1 and its domains and motifs. Residues targeted and mutated by
1100 CRISPR-Cas9 base editor are indicated with arrows.

1101 (B) Editing outcome for sgSUGP1_238: At t0 and in the absence of PB treatment E554Q
1102 dominates. This mutation depletes under PB treatment and E554K becomes the dominant
1103 mutation.

1104 (C) Editing outcome for sgSUGP1_188: PB treatment enriches for G603N. Inferred phenotypic
1105 mutations are indicated with a green background and inferred bystander mutations with a
1106 yellow background.

1107 (D) Sequence alignment of all human G-patch motifs involved in splicing with the NKRF G-
1108 patch motif included as a reference for structural comparison. Shaded residues indicate amino
1109 acids with more than 30% identity. Brace-helix and brace-loop, as identified in the NKR G-
1110 patch are marked above the aligned sequences. Positions of mutants identified in screen are
1111 also indicated. Sequence alignment was performed with JalView (v.2.11.2.5).

1112 (E) Identified splicing changes for mutant vs. control cell lines. Skipped exons and A3'SS are
1113 the most frequently observed splicing changes. Numbers are shown for junctions identified with
1114 rMATS with FDR > 0.01 and $|\Delta\text{PSI}| \geq 10$ (ΔPSI : PSI of mutant sample – PSI of control sample,
1115 where PSI: percent spliced in). RNA-seq data of total, polyA-selected RNA from three
1116 independent clonal cell lines treated for 3 h with DMSO. (A3'SS: alternative 3' splice site use;

1117 A5'SS: alternative 5' splice site use; MXE: mutually exclusive exon; RI: retained intron; SE:
1118 skipped exon.)

1119 (F) Sashimi plot for alternative 3' splice site usage in *TMEM14C* exon 2 (DMSO). The control
1120 cell line exclusively uses the distal 3' SS while the SUGP1 mutants also make use of a proximal
1121 3'SS. Representative traces for a single clonal cell line are shown (plot generated with IGV;
1122 alignment to Hg38).

1123 (G) RT-PCR and quantification for alternative 3' splice site usage for *TMEM14C* exon 2
1124 (DMSO). RNA extracted from eHAP FNLS cell lines – same monoclonal cell lines as for RNA-
1125 seq.

1126 *Statistical analysis for RT-PCR*: one-way ANOVA with Dunnett's for multiple comparison (two-
1127 sided, with control as reference) was performed with R and package multcomp (v.1.4-20); * p <
1128 0.05, ** p < 0.01, and *** p < 0.001; all with n = 3.

1129

1130

1131 Figure 5. RNA-seq analysis of mutants

1132 (A) Analysis of PB-induced splicing regulation in mutant vs. control cell lines. PB-resistant cell
1133 lines carrying mutations PHF5A 2xTL or SF3B1 T1080I at the PB binding pocket show very
1134 little change in splicing regulation compared to control cell lines or SUGP1 mutant cell lines.
1135 Numbers are shown for junctions identified with rMATS with FDR > 0.01 and $|\Delta\text{PSI}| \geq 10$. RNA-
1136 seq data of total, polyA-selected RNA from three independent clonal cell lines treated for 3 h
1137 with 2 nM PB or DMSO.

1138 (B) Overlap in cassette exons affected by PB treatment for all junctions observed in all three
1139 sample groups (control vs. SUGP1 E554K vs. SUGP1 G603N). 29% of differentially spliced
1140 cassette exons are affected in all three genetic backgrounds. SUGP1 mutants do not share
1141 more overlap than they individually share with the control sample. Splicing junctions had to be
1142 detected by rMATS with FDR < 0.01 to be included in analysis.

1143 (C) Overlap in alternative 3' splice site use affected by PB treatment for all junctions observed
1144 in all three sample groups (control vs. SUGP1 E554K vs. SUGP1 G603N). 23% of differentially
1145 spliced cassette exons are affected in all three genetic backgrounds. SUGP1 mutants do not

1146 share more overlap than they individually share with the control sample. Splicing junctions had
1147 to be detected by rMATS with FDR < 0.01 to be included in analysis.

1148 (D) Hierarchical clustering of differential splicing of alternative 3' splice sites for PB treatment,
1149 based on PSI (percent spliced in) changes. The heatmap represents Δ PSI values of A3'SS use
1150 upon treatment with PB at 2 nM for 3 h vs. DMSO as detected in total, polyA-selected RNA
1151 using rMATS. In contrast to mutants at the PB-binding interface, SUGP1 mutants E554K and
1152 G603N are susceptible to PB induced splicing changes. Predominantly, PB treatment results in
1153 increased and decreased use of the canonical 3'SS. Mutations in SUGP1 modulate observed
1154 phenotype. Only splicing junctions with FDR < 0.01 and $|\Delta$ PSI| \geq 10 were considered.

1155 (E) Hierarchical clustering of differential splicing of cassette exons for PB treatment. The
1156 heatmap represents Δ PSI values of cassette exons upon treatment with PB at 2 nM for 3 h vs.
1157 DMSO as detected in total, polyA-selected RNA from eHAP FNLS cells using rMATS. In
1158 contrast to mutants at the PB-binding interface, SUGP1 mutants E554K and G603N are
1159 susceptible to PB induced splicing changes. Predominantly, PB treatment results in increased
1160 exon skipping and mutations in SUGP1 modulate observed phenotype. Only splicing junctions
1161 with FDR < 0.01 and $|\Delta$ PSI| \geq 20 were considered.

1162 (F) Sashimi plot for alternative splicing of exon 16 in *RBM5* for 2 nM PB vs. DMSO treatment.
1163 The control cell line and the SUGP1 mutants switch to predominant exon skipping upon PB
1164 treatment. Representative traces for a single cell line each (plot generated with IGV; alignment
1165 to Hg38).

1166 (G) Sashimi plot for alternative splicing of exon 4 in *ORC6* for 2 nM PB vs. DMSO treatment.
1167 SUGP1 mutants show less exon skipping than control cell lines upon PB treatment.
1168 Representative traces for a single cell line each are shown (plot generated with IGV; alignment
1169 to Hg38).

1170

1171 Figure 6. SUGP1 interacts with DHX15.

1172 (A) miniTurbo proximity labeling using FLAG-SUGP1-miniTurboID G603N vs. wt overexpressed
1173 in HEK293T cells. Biotinylated proteins were identified with TMT-MS after enrichment with
1174 streptavidin beads. $-\log_{10}$ (p-value) is plotted against the \log_2 -fold change (LFC) in a volcano

1175 plot (dashed lines: cutoffs at $p < 0.05$ and $LFC > 0.5$). The only identified depleted factor is
1176 DHX15. SURF6 is a protein of the ribosomal biogenesis pathway.

1177 (B) AlphaFold2 prediction of SUGP1 (522-633), encompassing the G-patch motif flanked by
1178 α H6 and α H7, in complex with DHX15. To the right a close up is shown. The residues identified
1179 in our screen (E554 & G603, magenta) are at the interface with DHX15, while α H6 & α H7 are
1180 not predicted to interact with the helicase. ($n = 4$)

1181 (C-E) Domain organization and schematic representation of the MBP-*hs*SUGP1 variants with
1182 the introduced mutations colored in red. The different SUGP1 construct boundaries for G-patch
1183 (amino acid residues 548-611), α H6- α H7 (522-633) and α H4- α H7 (436-633), respectively, are
1184 indicated at the sides and features of the predicted secondary structure are depicted above.

1185 (D-E) Coomassie-stained gels of protein binding assays using purified MBP-*hs*SUGP1
1186 constructs and His₁₀-*hs*DHX15 Δ N. MBP-SUGP1 G-patch (D), and α H4- α H7 (E) with either
1187 wildtype (wt) protein sequence or carrying the indicated mutation were used as baits and His₆-
1188 MBP served as a control. Input (1.5% of total) and eluates (24% of total) were loaded.

1189 (F-G) Fluorescence polarization of FAM-labeled U₁₂ RNA with His₁₀-*hs*DHX15 Δ N in the
1190 absence or presence of MBP-SUGP1 G-patch (F) and α H4- α H7 (G) wt or mutants. The dashed
1191 line indicates 50% normalized polarization. Error bars represent standard deviations from the
1192 average values of triplicate measurements. RNA dissociation constants (K_d) with standard
1193 error of means (SEM) were derived from fitting the respective data by linear regression.

1194 (H) Initial ATPase activity rates of His₁₀-*hs*DHX15 Δ N in the absence or presence of MBP-
1195 *hs*SUGP1 G-patch wt or mutants at 250 μ M ATP. Error bars indicate standard deviations of
1196 three independent measurements, asterisks denote significance (one-way ANOVA with
1197 Tukey's) with ** $p < 0.01$, *** $p < 0.001$, and **** $p < 0.0001$.

1198

1199 Figure 7. Model for SUGP1-DHX15 and proofreading at early spliceosome assembly

1200 *Left panel:* On weak splice sites (either with a weak branchpoint sequence, PPT or 3' SS or a
1201 combination thereof) the transition from E complex to A complex is inhibited as PB binds to the
1202 U2 snRNP and prevents the full binding of the branch helix and recognition of the BP-A. These
1203 stalled spliceosomes are recognized by SUGP1-DHX15 and are discarded. Less mRNA is

1204 being produced in this scenario and more alternative mRNAs with skipped exons or alternative
1205 3' splice site choice result.

1206 *Right panel:* A mutation in SUGP1 can weaken SUGP1 interaction with DHX15, removing the
1207 proofreading & discard pathway, giving the cell “more time” to assembly A complex and to
1208 proceed with splicing.

1209

1210 SUPPLEMENTARY FIGURE LEGENDS

1211

1212 Figure S1. Spliceosome base editor screen

1213 (A) Lentiviral vectors used in this study. *Left*: Construct for generation of eHAP FNLS cell line
1214 by transduction and selection for blasticidin resistant cells exhibiting GFP fluorescence. *Right*:
1215 Vector for pooled library. The sgRNA is followed by a N₂₀-barcode which will uniquely label
1216 each sgRNA and can be read out during paired-end sequencing. The vector carries a
1217 puromycin resistance cassette for easy selection during the screen.

1218 (B) Schematic of CRISPR-Cas9 base editing. The sgRNA loaded on a nickase Cas9 (nCas9)
1219 targets a tethered ssDNA-specific deaminase to a chosen genomic locus. The deaminase then
1220 modifies all nucleotides within the editing window.

1221 (C) Benchmark test of eHAP1 FNLS cell line for four commonly used sgRNAs. Shown is the
1222 rate for C > T editing as well as for C > R transversion mutations six days post-transduction
1223 with the sgRNA and after selection for sgRNA carrying cells. Overall high rates of editing are
1224 observed for eHAP FNLS. Editing rates across replicates are very consistent. (n = 4, except
1225 HEK2 n=6)

1226 (D) Benchmark test of eHAP1 FNLS cell line. Shown are Sanger sequencing traces for the
1227 target region of EMX1 and HEK3 sgRNA. In the presence of the sgRNA the cytosines within
1228 the editing window (position 5 and 6, or 4 and 5 respectively) are modified.

1229 (E) Fraction of nucleotides that can be modified across the coding sequence targeted by the
1230 spliceosome sgRNA library with FNLS.

1231 (F) Predicted editing consequences per sgRNA from VEP when utilizing FNLS. ~70% of
1232 changes are predicted to be of high impact. Consequences were binned into categories based
1233 on most severe outcome with splice site acceptor/donor variant > nonsense > stop lost > start
1234 lost > missense > splice region variant > silent > intron variant > UTR variant.

1235 (G) Performance of sgRNAs targeting spliceosomal proteins, binned by predicted editing
1236 consequence. Non-targeting sgRNAs serve as a negative control. The dashed line marks the
1237 LFC for the bottom 5% of negative controls (LFC = -0.8814), percentage of sgRNAs falling
1238 below this threshold is indicated. Figure drawn in R with ggplot2 (v3.3.6) and ggridges (v0.5.3).

1239

1240

1241 Figure S2 Validation and mapping experiments

1242 (A) Individual sgRNAs and their performance in the confirmation assay. Measurements are from
1243 three independent transductions (n=3). Student's t-Test (paired) with *P* value * $p < 0.05$, ** $p <$
1244 0.01 , and *** $p < 0.001$, respectively.

1245 (B) Sum of conversion per each position within the protospacer, for 23 sgRNAs validated for
1246 hypersensitivity to PB. The position of the C is indicated along the x axis, with 1 corresponding
1247 to the first nucleotide of the protospacer and 21-23 corresponding to the PAM. The editing
1248 window (3-8) is shown in gray. Lines indicate median of edits at that position across all 23
1249 sgRNAs.

1250 (C) Location of PB sensitive mutations in SF1 mapped to structure of chimeric SF1 SURP
1251 binding region fused to SF3A1 SURP1. SF1 residues S315 and L316 are targeted by
1252 sgSF1_265, which gives rise to PB sensitivity. The target lies within the SF1 SURP binding
1253 region and forms part of the hydrophobic interface with SF3A1 SURP1. sgSF3A1_121 and
1254 sgSF3A1_283 result in mutation of SF3A1 SURP1 residues S110 and R50, respectively, which
1255 results in PB sensitivity. All sgRNA targeted residues are shown in magenta. (PDB: 7VH9)

1256 (D) Location of the SURP1 domain of SF3A1 in the B^{act} complex, the earliest stage of
1257 spliceosome assembly it has been visualized in. PB hypersensitive mutations of SF3A1 target
1258 R50 and S110, which locate to the SURP1 domain. Both residues are at this stage in proximity
1259 to XAB2/SYF1 and CRINKL/SYF3 which are part of "bridge 2" as described by Haselbach *et al.*
1260 (2018). (PDB: 6FF7)

1261 (E+F) Six sgRNAs targeting CDC40/hPrp17 give rise to PB sensitivity. (PDB: 5XJC) (E) Three
1262 target the N-terminal domain of CDC40 at the flexible N-terminus (S14 and S16) as well as at
1263 P95 and G113. P95 is in close contact to the PPIL1 domain, while G113 is at the interface to
1264 RBM22. (F) Three more sgRNAs target the C-terminal WD40 domain of CDC40. The target
1265 sites are located in loops which face away from the catalytic core.

1266

1267 Figure S3. Analysis of mutations in PHF5A

1268 (A) Editing outcome for sgPHF5A_7: In the absence of PB the sgRNA results in a K29N
1269 mutation. PB treatment further enriches for this mutation. Bystander mutations at D27 may
1270 occur but do not strongly enrich.

1271 (B) Editing outcome for sgPHF5A_21: In the absence of PB some mutations occur at E74. PB
1272 treatment enriches for an E74D mutation (with E74N also showing some enrichment vs. the
1273 DMSO control sample).

1274 (C) Editing outcome for sgPHF5A_47: In the absence of PB the 3'SS of exon 3 is mutated. PB
1275 treatment enriches for mutations at D27.

1276 (D) Editing outcome for sgPHF5A_26: In the absence of PB mutations occur at S67. PB
1277 treatment enriches for an S67C which is present at a similar prevalence as S67F at t15.

1278 (E) Comparison of predicted mutations in PHF5A with actual confirmed mutations in PHF5A.
1279 Deep sequencing of the target region allows for the precise identification of mutations likely
1280 responsible for phenotype (PB resistance). This shows that while sgRNAs can predict the
1281 region where mutations occur, in this instance only D27 could be confirmed as a mutation site.
1282 The four other sgRNAs resulted in mutations proximal to the predicted editing sites.

1283

1284 Figure S4. Clonal cell line generation and analysis

1285 (A) Schematic for generation of monoclonal eHAP FNLS cell lines carrying mutations in splicing
1286 factors. All cell lines were genotyped and verified to be haploid.

1287 (B) Sixty hour cell proliferation profiling (CellTiter-AQueous cellular viability and cytotoxicity
1288 assay) of control eHAP FNLS cell line expressing non-targeting sgRNA and monoclonal cell
1289 lines carrying either SUGP1 E554K or SUGP1 G603N mutation to PB. Error bars indicate s.d. n
1290 = 3 (average of two technical replicates for independent clonal cell lines).

1291 (C) Cell cycle analysis for eHAP FNLS upon treatment with 2 nM PB. After 4 h an increase in
1292 G2% suggests cell cycle arrest and death. Cell cycle analysis was performed on ethanol fixated
1293 cells by staining with propidium iodide after RNase treatment (5 µg RNase A at RT for 30 min
1294 per max. 1e6 cells).

1295 (D) MA-plots for RNA-seq comparing control cell line transcript mean counts vs. mutant cell
1296 lines under DMSO treatment. Mutations do not appear to affect the transcriptome.

1297 (E) Sashimi plot for alternative 3' splice site usage in *ENOSF1* exon 11 (DMSO). The control
1298 cell line exclusively uses the distal 3'SS while the SUGP1 mutants also make use of a proximal
1299 3'SS. Representative traces are shown (plot generated with IGV with only junctions ≥ 5 reads
1300 shown; alignment to Hg38) and junctions of interest are emphasized.

1301 (F) RT-PCR and quantification for alternative 3' splice site usage for *ENOSF1* exon 11
1302 (DMSO). RNA extracted from eHAP FNLS cell lines – same monoclonal cell lines as for RNA-
1303 seq.

1304 (G) PAGE as used for quantification in (F and 5G). Shown is also the RT- control (pooled
1305 samples for each genetic background), which shows no amplification.

1306 *Statistical analysis for RT-PCR*: one-way ANOVA with Dunnett's for multiple comparison (two-
1307 sided, with control as reference) was performed with R and package multcomp (v.1.4-20); * $p <$
1308 0.05, ** $p < 0.01$, and *** $p < 0.001$; all with $n = 3$.

1309

1310 Figure S5. SUGP1 mutant splicing analysis

1311 (A) Expanded view of Figure 5C focusing on SUGP1 mutants.

1312 (B) Quantification of differential splicing in eHAP FNLS control or mutant cell lines by RT-PCR
1313 corresponding to observations from RNA-seq as shown in Figure 5 and S5D. Shown is the
1314 change in cassette exon splicing upon treatment with PB vs. DMSO. *Top*: PB induces
1315 increased exon skipping for *RBM5* exon 16 to the same degree in control as well as the
1316 SUGP1 mutant cell lines. *Bottom*: PB induces increased exon skipping for *ORC6* exon 5.
1317 SUGP1 mutation modulates this phenotype, with the G603N mutant cell lines showing a
1318 significant decrease in exon 5 skipping compared to the control cell lines. Statistical
1319 significance is only shown for mutant samples vs. control (= reference).

1320 (C) Representative PAGE as used for quantification in (B).

1321 (D) Cartoon representation of SUGP1 and its domain and motif organisation. α -helices
1322 identified with AlphaFold2 and in proximity to the G-patch motif are shown in orange (α H4-5,
1323 α H6, and α H7). Several cancer mutations locate to these α -helices or their vicinity (grey arrows
1324 and residue numbers).

1325 (E) Western blot for overexpression assays using HA-SUGP1 or HA-SUGP1 mutants as shown
1326 in (G-H). 1 μ g plasmid was transfected into HEK293T cells and RNA or protein samples were
1327 extracted 48 h later. Membrane had to be cropped between samples L570E and $\Delta\alpha$ H4-5 (non-
1328 discussed sample).

1329 (G) RT-PCR and quantification for alternative 3' splice site usage in *ENOSF1* exon 11 upon
1330 SUGP1 wt or mutant protein overexpression (48 h) in HEK293T cells. Overexpression of
1331 SUGP1 wt does not influence splicing outcome. α H6 shows an equally strong phenotype as G-
1332 patch point mutants. A representative example of the PAGE used for quantification is shown.

1333 (H) RT-PCR and quantification for alternative 3' splice site usage in *ENOSF1* exon 11 upon
1334 SUGP1 wt or mutant protein overexpression (48 h) in HEK293T cells. Overexpression of
1335 SUGP1 wt does not influence splicing outcome. All mutants affect splicing 3' splice site choice,
1336 with α H4-5 and α H6 showing a similar phenotype as G603N. A representative example of the
1337 PAGE used for quantification is shown.

1338 *Statistical analysis for RT-PCR*: one-way ANOVA with Dunnett's (*ENOSF1*, *TMEM14C* – with
1339 control as reference) or Tukey's (*RBM5*, *ORC6*) for multiple comparison (two-sided) was
1340 performed with R and package multcomp (v.1.4-20); * $p < 0.05$, ** $p < 0.01$, and *** $p < 0.001$;
1341 all with $n = 3$.

1342

1343 Figure S6. Proximity labeling experiments

1344 (A) Schematic for BioID experiments.

1345 (B) Optimization of labeling using SUGP1-miniTurboID overexpression in HEK293T cells.
1346 Different time points and biotin concentrations were compared to obtain strong labeling within a
1347 short time frame. When no SUGP1-miniTurboID was transfected only background levels of
1348 endogenously biotinylated proteins are observed.

1349 (C) miniTurbo proximity labeling using SUGP1-miniTurboID L570E vs. wt overexpressed in
1350 HEK293T cells. Biotinylated proteins were identified with TMT-MS after enrichment with
1351 streptavidin beads. $-\log_{10}(p\text{-value})$ is plotted against the \log_2 -fold change (LFC) in a volcano
1352 plot (dashed lines: cutoffs at $p < 0.05$ and $LFC > 0.5$). All depleted or enriched proteins are
1353 labelled and spliceosome associated factors are underlined. SNRNP48 (associated with the

1354 minor spliceosome) and DHX15 are the only spliceosomal proteins that show a significant
1355 change, with both depleted. (n = 4)

1356 (D) Domain organization and schematic representation of the MBP-*hsSUGP1* variants with the
1357 introduced mutations colored in red for construct α H6- α H7 (522-633).

1358 (E) Coomassie-stained gels of protein binding assays using purified MBP-*hsSUGP1* construct
1359 and His₁₀-*hsDHX15* Δ N. MBP-SUGP1 α H6- α H7 with either wildtype (wt) protein sequence or
1360 carrying the indicated mutation were used as baits and His₆-MBP served as a control. Input
1361 (1.5% of total) and eluates (24% of total) were loaded.

1362 (F) Fluorescence polarization of FAM-labeled U₁₂ RNA with His₁₀-*hsDHX15* Δ N in the absence
1363 or presence of MBP-SUGP1 α H6- α H7 wt or mutants. The dashed line indicates 50%
1364 normalized polarization. Error bars represent standard deviations from the average values of
1365 triplicate measurements. RNA dissociation constants (K_d) with standard error of means (SEM)
1366 were derived from fitting the respective data by linear regression.

1367

1368 REFERENCES

1369

- 1370 Alsafadi, S., Dayot, S., Tarin, M., Houy, A., Bellanger, D., Cornella, M., Wassef, M., Waterfall,
1371 J.J., Lehnert, E., Roman-Roman, S., *et al.* (2021). Genetic alterations of SUGP1 mimic mutant-
1372 SF3B1 splice pattern in lung adenocarcinoma and other cancers. *Oncogene* 40, 85-96.
- 1373 Anzalone, A.V., Koblan, L.W., and Liu, D.R. (2020). Genome editing with CRISPR-Cas
1374 nucleases, base editors, transposases and prime editors. *Nat Biotechnol* 38, 824-844.
- 1375 Beigl, T.B., Kjosås, I., Seljeseth, E., Glomnes, N., and Aksnes, H. (2020). Efficient and crucial
1376 quality control of HAP1 cell ploidy status. *Biology open* 9, bio057174.
- 1377 Bejar, R. (2016). Splicing Factor Mutations in Cancer. *Advances in experimental medicine and*
1378 *biology* 907, 215-228.
- 1379 Blencowe, B.J. (2017). The Relationship between Alternative Splicing and Proteomic
1380 Complexity. *Trends in biochemical sciences* 42, 407-408.
- 1381 Boettcher, M., Covarrubias, S., Biton, A., Blau, J., Wang, H., Zaitlen, N., and McManus, M.T.
1382 (2019). Tracing cellular heterogeneity in pooled genetic screens via multi-level barcoding. *BMC*
1383 *Genomics* 20, 107.
- 1384 Branon, T.C., Bosch, J.A., Sanchez, A.D., Udeshi, N.D., Svinkina, T., Carr, S.A., Feldman, J.L.,
1385 Perrimon, N., and Ting, A.Y. (2018). Efficient proximity labeling in living cells and organisms
1386 with TurboID. *Nat Biotechnol* 36, 880-887.
- 1387 Brosi, R., Hauri, H.P., and Krämer, A. (1993). Separation of splicing factor SF3 into two
1388 components and purification of SF3a activity. *Journal of Biological Chemistry* 268, 17640-
1389 17646.
- 1390 Burgess, S.M., and Guthrie, C. (1993). A mechanism to enhance mRNA splicing fidelity: the
1391 RNA-dependent ATPase Prp16 governs usage of a discard pathway for aberrant lariat
1392 intermediates. *Cell* 73, 1377-1391.

- 1393 Clauser, K.R., Baker, P., and Burlingame, A.L. (1999). Role of accurate mass measurement
1394 (+/- 10 ppm) in protein identification strategies employing MS or MS/MS and database
1395 searching. *Anal Chem* *71*, 2871-2882.
- 1396 Cretu, C., Agrawal, A.A., Cook, A., Will, C.L., Fekkes, P., Smith, P.G., Luhrmann, R., Larsen,
1397 N., Buonamici, S., and Pena, V. (2018a). Structural Basis of Splicing Modulation by Antitumor
1398 Macrolide Compounds. *Mol Cell* *70*, 265-273 e268.
- 1399 Cretu, C., Agrawal, A.A., Cook, A., Will, C.L., Fekkes, P., Smith, P.G., Luhrmann, R., Larsen,
1400 N., Buonamici, S., and Pena, V. (2018b). Structural Basis of Splicing Modulation by Antitumor
1401 Macrolide Compounds. *Molecular Cell* *70*, 265-273.e268.
- 1402 Cretu, C., Gee, P., Liu, X., Agrawal, A., Nguyen, T.V., Ghosh, A.K., Cook, A., Jurica, M.,
1403 Larsen, N.A., and Pena, V. (2021). Structural basis of intron selection by U2 snRNP in the
1404 presence of covalent inhibitors. *Nat Commun* *12*, 4491.
- 1405 Cuella-Martin, R., Hayward, S.B., Fan, X., Chen, X., Huang, J.W., Taglialatela, A., Leuzzi, G.,
1406 Zhao, J., Rabadan, R., Lu, C., *et al.* (2021). Functional interrogation of DNA damage response
1407 variants with base editing screens. *Cell* *184*, 1081-1097 e1019.
- 1408 Dobin, A., Davis, C.A., Schlesinger, F., Drenkow, J., Zaleski, C., Jha, S., Batut, P., Chaisson,
1409 M., and Gingeras, T.R. (2013). STAR: ultrafast universal RNA-seq aligner. *Bioinformatics* *29*,
1410 15-21.
- 1411 Doench, J.G., Fusi, N., Sullender, M., Hegde, M., Vaimberg, E.W., Donovan, K.F., Smith, I.,
1412 Tothova, Z., Wilen, C., Orchard, R., *et al.* (2016). Optimized sgRNA design to maximize activity
1413 and minimize off-target effects of CRISPR-Cas9. *Nat Biotechnol* *34*, 184-191.
- 1414 Essletzbichler, P., Konopka, T., Santoro, F., Chen, D., Gapp, B.V., Kralovics, R.,
1415 Brummelkamp, T.R., Nijman, S.M., and Burckstummer, T. (2014). Megabase-scale deletion
1416 using CRISPR/Cas9 to generate a fully haploid human cell line. *Genome Res* *24*, 2059-2065.
- 1417 Fica, S.M., Oubridge, C., Wilkinson, M.E., Newman, A.J., and Nagai, K. (2019). A human
1418 postcatalytic spliceosome structure reveals essential roles of metazoan factors for exon
1419 ligation. *Science* *363*, 710-714.
- 1420 Gamboa Lopez, A., Allu, S.R., Mendez, P., Chandrashekar Reddy, G., Maul-Newby, H.M.,
1421 Ghosh, A.K., and Jurica, M.S. (2021). Herboxidiene Features That Mediate Conformation-
1422 Dependent SF3B1 Interactions to Inhibit Splicing. *ACS Chem Biol* *16*, 520-528.
- 1423 Gohr, A., and Irimia, M. (2019). Matt: Unix tools for alternative splicing analysis. *Bioinformatics*
1424 *35*, 130-132.
- 1425 Guan, W., Orellana, K.G., Stephens, R.F., Zhorov, B.S., and Spafford, J.D. (2022). A lysine
1426 residue from an extracellular turret switches the ion preference in a Cav3 T-Type channel from
1427 calcium to sodium ions. *J Biol Chem*, 102621.
- 1428 Haffke, M., Marek, M., Pelosse, M., Diebold, M.L., Schlattner, U., Berger, I., and Romier, C.
1429 (2015). Characterization and production of protein complexes by co-expression in *Escherichia*
1430 *coli*. *Methods Mol Biol* *1261*, 63-89.
- 1431 Hanna, R.E., Hegde, M., Fagre, C.R., DeWeirdt, P.C., Sangree, A.K., Szegletes, Z., Griffith, A.,
1432 Feeley, M.N., Sanson, K.R., Baidi, Y., *et al.* (2021). Massively parallel assessment of human
1433 variants with base editor screens. *Cell* *184*, 1064-1080 e1020.
- 1434 Haselbach, D., Komarov, I., Agafonov, D.E., Hartmuth, K., Graf, B., Dybkov, O., Urlaub, H.,
1435 Kastner, B., Luhrmann, R., and Stark, H. (2018). Structure and Conformational Dynamics of the
1436 Human Spliceosomal Bact Complex. *Cell* *172*, 454-464.e411.
- 1437 Hemsley, A., Arnheim, N., Toney, M.D., Cortopassi, G., and Galas, D.J. (1989). A simple
1438 method for site-directed mutagenesis using the polymerase chain reaction. *Nucleic Acids Res*
1439 *17*, 6545-6551.
- 1440 Irimia, M., and Roy, S.W. (2008). Evolutionary convergence on highly-conserved 3' intron
1441 structures in intron-poor eukaryotes and insights into the ancestral eukaryotic genome. *PLoS*
1442 *Genet* *4*, e1000148.
- 1443 Jumper, J., Evans, R., Pritzel, A., Green, T., Figurnov, M., Ronneberger, O., Tunyasuvunakool,
1444 K., Bates, R., Zidek, A., Potapenko, A., *et al.* (2021). Highly accurate protein structure
1445 prediction with AlphaFold. *Nature* *596*, 583-589.
- 1446 Kent, W.J. (2002). BLAT---The BLAST-Like Alignment Tool. *Genome Research* *12*, 656-664.
- 1447 Kluesner, M.G., Lahr, W.S., Lonetree, C.L., Smeester, B.A., Qiu, X., Slipek, N.J., Claudio
1448 Vazquez, P.N., Pitzen, S.P., Pomeroy, E.J., Vignes, M.J., *et al.* (2021). CRISPR-Cas9 cytidine

- 1449 and adenosine base editing of splice-sites mediates highly-efficient disruption of proteins in
1450 primary and immortalized cells. *Nat Commun* 12, 2437.
- 1451 Kluesner, M.G., Nedveck, D.A., Lahr, W.S., Garbe, J.R., Abrahante, J.E., Webber, B.R., and
1452 Moriarity, B.S. (2018). EditR: A Method to Quantify Base Editing from Sanger Sequencing.
1453 *CRISPR J* 1, 239-250.
- 1454 Koodathingal, P., Novak, T., Piccirilli, J.A., and Staley, J.P. (2010). The DEAH box ATPases
1455 Prp16 and Prp43 cooperate to proofread 5' splice site cleavage during pre-mRNA splicing. *Mol*
1456 *Cell* 39, 385-395.
- 1457 Koodathingal, P., and Staley, J.P. (2013). Splicing fidelity: DEAD/H-box ATPases as molecular
1458 clocks. *RNA Biol* 10, 1073-1079.
- 1459 Labun, K., Montague, T.G., Krause, M., Torres Cleuren, Y.N., Tjeldnes, H., and Valen, E.
1460 (2019). CHOPCHOP v3: expanding the CRISPR web toolbox beyond genome editing. *Nucleic*
1461 *Acids Res* 47, W171-W174.
- 1462 Le Hir, H., Sauliere, J., and Wang, Z. (2016). The exon junction complex as a node of post-
1463 transcriptional networks. *Nat Rev Mol Cell Biol* 17, 41-54.
- 1464 Li, Y.I., van de Geijn, B., Raj, A., Knowles, D.A., Petti, A.A., Golan, D., Gilad, Y., and Pritchard,
1465 J.K. (2016). RNA splicing is a primary link between genetic variation and disease. *Science* 352,
1466 600-604.
- 1467 Liao, Y., Smyth, G.K., and Shi, W. (2019). The R package Rsubread is easier, faster, cheaper
1468 and better for alignment and quantification of RNA sequencing reads. *Nucleic acids research*
1469 47, e47-e47.
- 1470 Liu, Z., Zhang, J., Sun, Y., Perea-Chamblee, T.E., Manley, J.L., and Rabadan, R. (2020). Pan-
1471 cancer analysis identifies mutations in SUGP1 that recapitulate mutant SF3B1 splicing
1472 dysregulation. *Proc Natl Acad Sci U S A* 117, 10305-10312.
- 1473 Love, M.I., Huber, W., and Anders, S. (2014). Moderated estimation of fold change and
1474 dispersion for RNA-seq data with DESeq2. *Genome Biol* 15, 550.
- 1475 Martin, A., Schneider, S., and Schwer, B. (2002). Prp43 is an essential RNA-dependent
1476 ATPase required for release of lariat-intron from the spliceosome. *J Biol Chem* 277, 17743-
1477 17750.
- 1478 Maul-Newby, H.M., Amorello, A.N., Sharma, T., Kim, J.H., Modena, M.S., Prichard, B.E., and
1479 Jurica, M.S. (2022). A model for DHX15 mediated disassembly of A-complex spliceosomes.
1480 *RNA (New York, NY)* 28, 583-595.
- 1481 Mayas, R.M., Maita, H., Semlow, D.R., and Staley, J.P. (2010). Spliceosome discards
1482 intermediates via the DEAH box ATPase Prp43p. *Proc Natl Acad Sci U S A* 107, 10020-10025.
- 1483 Mayas, R.M., Maita, H., and Staley, J.P. (2006). Exon ligation is proofread by the DEXD/H-box
1484 ATPase Prp22p. *Nat Struct Mol Biol* 13, 482-490.
- 1485 McLaren, W., Gil, L., Hunt, S.E., Riat, H.S., Ritchie, G.R., Thormann, A., Flicek, P., and
1486 Cunningham, F. (2016). The Ensembl Variant Effect Predictor. *Genome Biol* 17, 122.
- 1487 Mehmood, A., Laiho, A., Venalainen, M.S., McGlinchey, A.J., Wang, N., and Elo, L.L. (2020).
1488 Systematic evaluation of differential splicing tools for RNA-seq studies. *Brief Bioinform* 21,
1489 2052-2065.
- 1490 Nameki, N., Takizawa, M., Suzuki, T., Tani, S., Kobayashi, N., Sakamoto, T., Muto, Y., and
1491 Kuwasako, K. (2022). Structural basis for the interaction between the first SURP domain of the
1492 SF3A1 subunit in U2 snRNP and the human splicing factor SF1. *Protein Sci* 31, e4437.
- 1493 Perez-Riverol, Y., Bai, J., Bandla, C., Garcia-Seisdedos, D., Hewapathirana, S.,
1494 Kamatchinathan, S., Kundu, D.J., Prakash, A., Frericks-Zipper, A., Eisenacher, M., *et al.*
1495 (2022). The PRIDE database resources in 2022: a hub for mass spectrometry-based
1496 proteomics evidences. *Nucleic Acids Res* 50, D543-D552.
- 1497 Pinello, L., Canver, M.C., Hoban, M.D., Orkin, S.H., Kohn, D.B., Bauer, D.E., and Yuan, G.C.
1498 (2016). Analyzing CRISPR genome-editing experiments with CRISPResso. *Nat Biotechnol* 34,
1499 695-697.
- 1500 Rossi, A.M., and Taylor, C.W. (2011). Analysis of protein-ligand interactions by fluorescence
1501 polarization. *Nat Protoc* 6, 365-387.
- 1502 Sales-Lee, J., Perry, D.S., Bowser, B.A., Diedrich, J.K., Rao, B., Beusch, I., Yates, J.R., 3rd,
1503 Roy, S.W., and Madhani, H.D. (2021). Coupling of spliceosome complexity to intron diversity.
1504 *Curr Biol* 31, 4898-4910 e4894.

- 1505 Sánchez-Rivera, F.J., Diaz, B.J., Kastenhuber, E.R., Schmidt, H., Katti, A., Kennedy, M., Tem,
1506 V., Ho, Y.-J., Leibold, J., Paffenholz, S.V., *et al.* (2022). Base editing sensor libraries for high-
1507 throughput engineering and functional analysis of cancer-associated single nucleotide variants.
1508 *Nature biotechnology* *40*, 862-873.
- 1509 Semlow, D.R., and Staley, J.P. (2012). Staying on message: ensuring fidelity in pre-mRNA
1510 splicing. *Trends in biochemical sciences* *37*, 263-273.
- 1511 Shen, S., Park, J.W., Lu, Z.-X., Lin, L., Henry, M.D., Wu, Y.N., Zhou, Q., and Xing, Y. (2014a).
1512 rMATS: robust and flexible detection of differential alternative splicing from replicate RNA-Seq
1513 data. *Proc Natl Acad Sci U S A* *111*, E5593-5601.
- 1514 Shen, S., Park, J.W., Lu, Z.X., Lin, L., Henry, M.D., Wu, Y.N., Zhou, Q., and Xing, Y. (2014b).
1515 rMATS: robust and flexible detection of differential alternative splicing from replicate RNA-Seq
1516 data. *Proc Natl Acad Sci U S A* *111*, E5593-5601.
- 1517 Studer, M.K., Ivanovic, L., Weber, M.E., Marti, S., and Jonas, S. (2020a). Structural basis for
1518 DEAH-helicase activation by G-patch proteins. *Proc Natl Acad Sci U S A* *117*, 7159-7170.
- 1519 Studer, M.K., Ivanović, L., Weber, M.E., Marti, S., and Jonas, S. (2020b). Structural basis for
1520 DEAH-helicase activation by G-patch proteins. *Proceedings of the National Academy of*
1521 *Sciences of the United States of America* *117*, 7159-7170.
- 1522 Tanaka, N., Aronova, A., and Schwer, B. (2007). Ntr1 activates the Prp43 helicase to trigger
1523 release of lariat-intron from the spliceosome. *Genes Dev* *21*, 2312-2325.
- 1524 Teng, T., Tsai, J.H., Puyang, X., Seiler, M., Peng, S., Prajapati, S., Aird, D., Buonamici, S.,
1525 Caleb, B., Chan, B., *et al.* (2017a). Splicing modulators act at the branch point adenosine
1526 binding pocket defined by the PHF5A-SF3b complex. *Nat Commun* *8*, 15522.
- 1527 Teng, T., Tsai, J.H., Puyang, X., Seiler, M., Peng, S., Prajapati, S., Aird, D., Buonamici, S.,
1528 Caleb, B., Chan, B., *et al.* (2017b). Splicing modulators act at the branch point adenosine
1529 binding pocket defined by the PHF5A-SF3b complex. *Nature communications* *8*, 15522-15522.
- 1530 Tholen, J., Razew, M., Weis, F., and Galej, W.P. (2022). Structural basis of branch site
1531 recognition by the human spliceosome. *Science* *375*, 50-57.
- 1532 Tsai, R.-T., Fu, R.-H., Yeh, F.-L., Tseng, C.-K., Lin, Y.-C., Huang, Y.-H., and Cheng, S.-C.
1533 (2005). Spliceosome disassembly catalyzed by Prp43 and its associated components Ntr1 and
1534 Ntr2. *Genes Dev* *19*, 2991-3003.
- 1535 Wahl, M.C., Will, C.L., and Luhrmann, R. (2009a). The spliceosome: design principles of a
1536 dynamic RNP machine. *Cell* *136*, 701-718.
- 1537 Wahl, M.C., Will, C.L., and Lührmann, R. (2009b). The spliceosome: design principles of a
1538 dynamic RNP machine. *Cell* *136*, 701-718.
- 1539 Wang, L., Wang, S., and Li, W. (2012). RSeQC: quality control of RNA-seq experiments.
1540 *Bioinformatics* *28*, 2184-2185.
- 1541 Warkocki, Z., Schneider, C., Mozaffari-Jovin, S., Schmitzova, J., Hobartner, C., Fabrizio, P.,
1542 and Luhrmann, R. (2015). The G-patch protein Spp2 couples the spliceosome-stimulated
1543 ATPase activity of the DEAH-box protein Prp2 to catalytic activation of the spliceosome. *Genes*
1544 *Dev* *29*, 94-107.
- 1545 Wilkinson, M.E., Charenton, C., and Nagai, K. (2020). RNA Splicing by the Spliceosome. *Annu*
1546 *Rev Biochem* *89*, 359-388.
- 1547 Wu, G., Fan, L., Edmonson, M.N., Shaw, T., Boggs, K., Easton, J., Rusch, M.C., Webb, T.R.,
1548 Zhang, J., and Potter, P.M. (2018). Inhibition of SF3B1 by molecules targeting the spliceosome
1549 results in massive aberrant exon skipping. *RNA* *24*, 1056-1066.
- 1550 Yokoi, A., Kotake, Y., Takahashi, K., Kadowaki, T., Matsumoto, Y., Minoshima, Y., Sugi, N.H.,
1551 Sagane, K., Hamaguchi, M., Iwata, M., *et al.* (2011). Biological validation that SF3b is a target
1552 of the antitumor macrolide pladienolide. *FEBS Journal* *278*, 4870-4880.
- 1553 Yoshimi, A., Lin, K.T., Wiseman, D.H., Rahman, M.A., Pastore, A., Wang, B., Lee, S.C., Micol,
1554 J.B., Zhang, X.J., de Botton, S., *et al.* (2019). Coordinated alterations in RNA splicing and
1555 epigenetic regulation drive leukaemogenesis. *Nature* *574*, 273-277.
- 1556 Zafra, M.P., Schatoff, E.M., Katti, A., Foronda, M., Breinig, M., Schweitzer, A.Y., Simon, A.,
1557 Han, T., Goswami, S., Montgomery, E., *et al.* (2018a). Optimized base editors enable efficient
1558 editing in cells, organoids and mice. *Nat Biotechnol* *36*, 888-893.
- 1559 Zafra, M.P., Schatoff, E.M., Katti, A., Foronda, M., Breinig, M., Schweitzer, A.Y., Simon, A.,
1560 Han, T., Goswami, S., Montgomery, E., *et al.* (2018b). Optimized base editors enable efficient
1561 editing in cells, organoids and mice. *Nature biotechnology* *36*, 888-893.

1562 Zhang, J., Ali, A.M., Lieu, Y.K., Liu, Z., Gao, J., Rabadan, R., Raza, A., Mukherjee, S., and
1563 Manley, J.L. (2019). Disease-Causing Mutations in SF3B1 Alter Splicing by Disrupting
1564 Interaction with SUGP1. *Mol Cell* 76, 82-95 e87.
1565 Zhang, X., Yan, C., Zhan, X., Li, L., Lei, J., and Shi, Y. (2018). Structure of the human activated
1566 spliceosome in three conformational states. *Cell Res* 28, 307-322.
1567 Zhang, Z., Rigo, N., Dybkov, O., Fourmann, J.-B., Will, C.L., Kumar, V., Urlaub, H., Stark, H.,
1568 and Lührmann, R. (2021). Structural insights into how Prp5 proofreads the pre-mRNA branch
1569 site. *Nature* 596, 296-300.
1570 Zhang, Z., Will, C.L., Bertram, K., Dybkov, O., Hartmuth, K., Agafonov, D.E., Hofele, R., Urlaub,
1571 H., Kastner, B., Luhrmann, R., *et al.* (2020a). Molecular architecture of the human 17S U2
1572 snRNP. *Nature* 583, 310-313.
1573 Zhang, Z., Will, C.L., Bertram, K., Dybkov, O., Hartmuth, K., Agafonov, D.E., Hofele, R., Urlaub,
1574 H., Kastner, B., Lührmann, R., *et al.* (2020b). Molecular architecture of the human 17S U2
1575 snRNP. *Nature* 583, 310-313.
1576

Figure 1

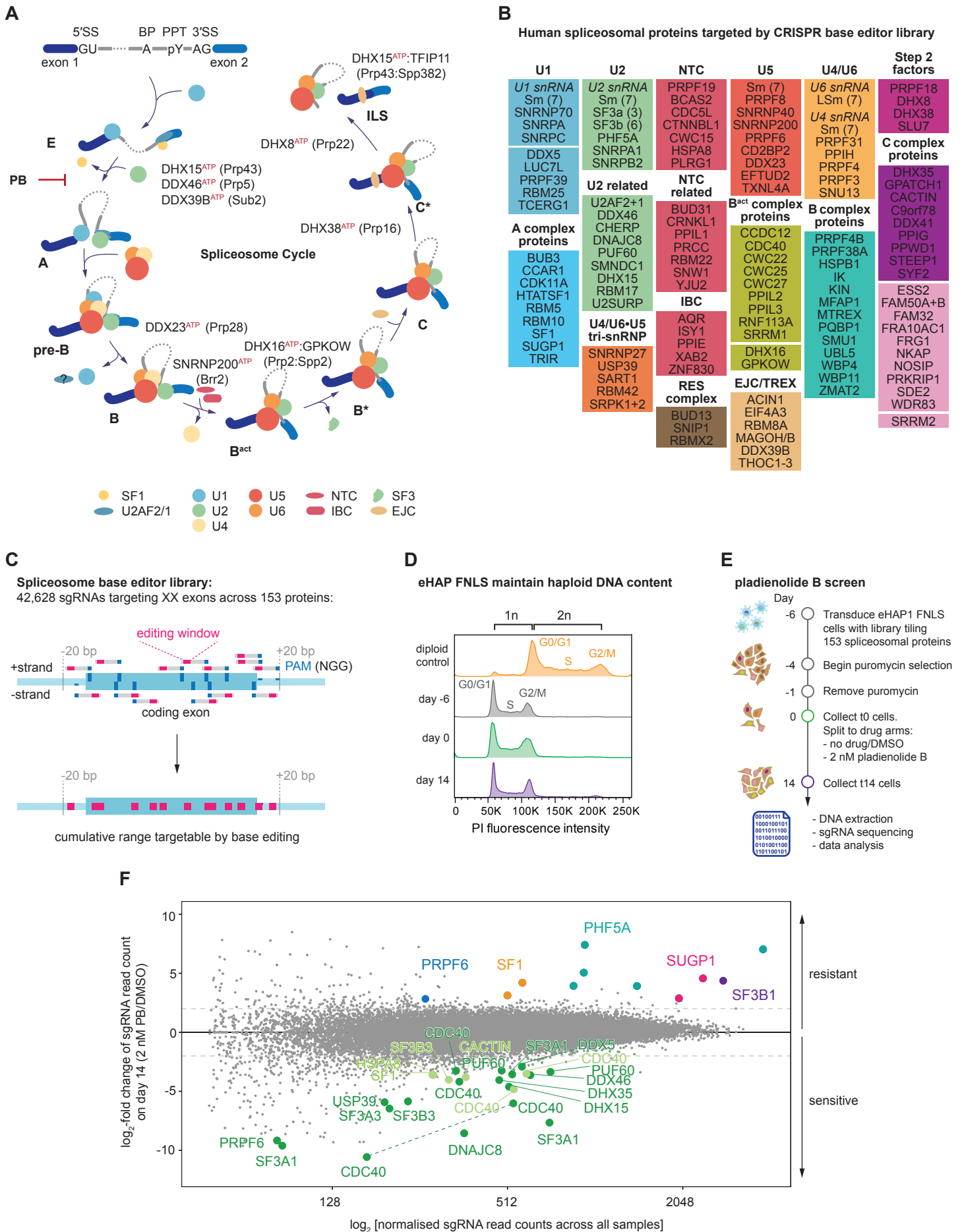


Figure 2

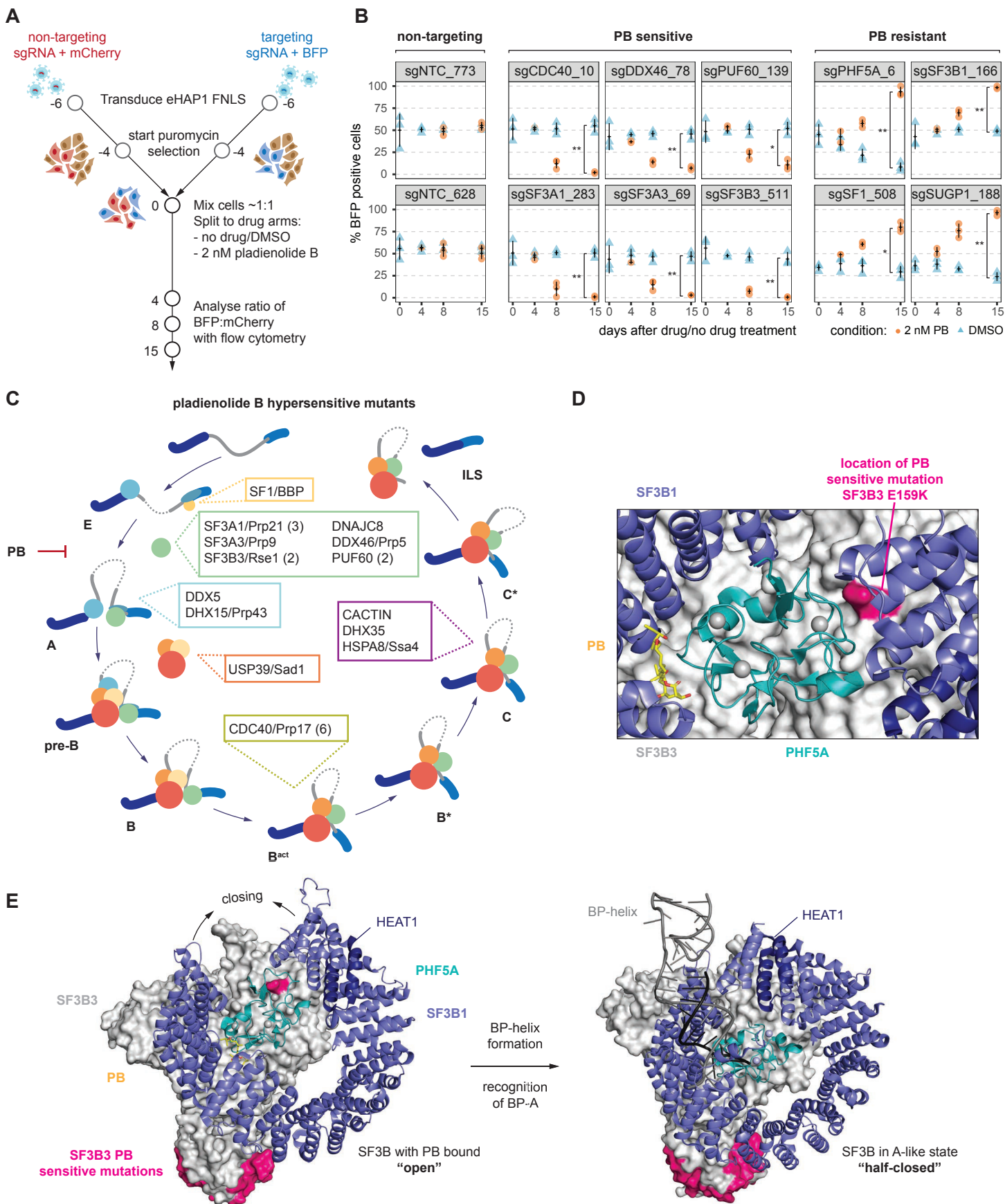


Figure 3

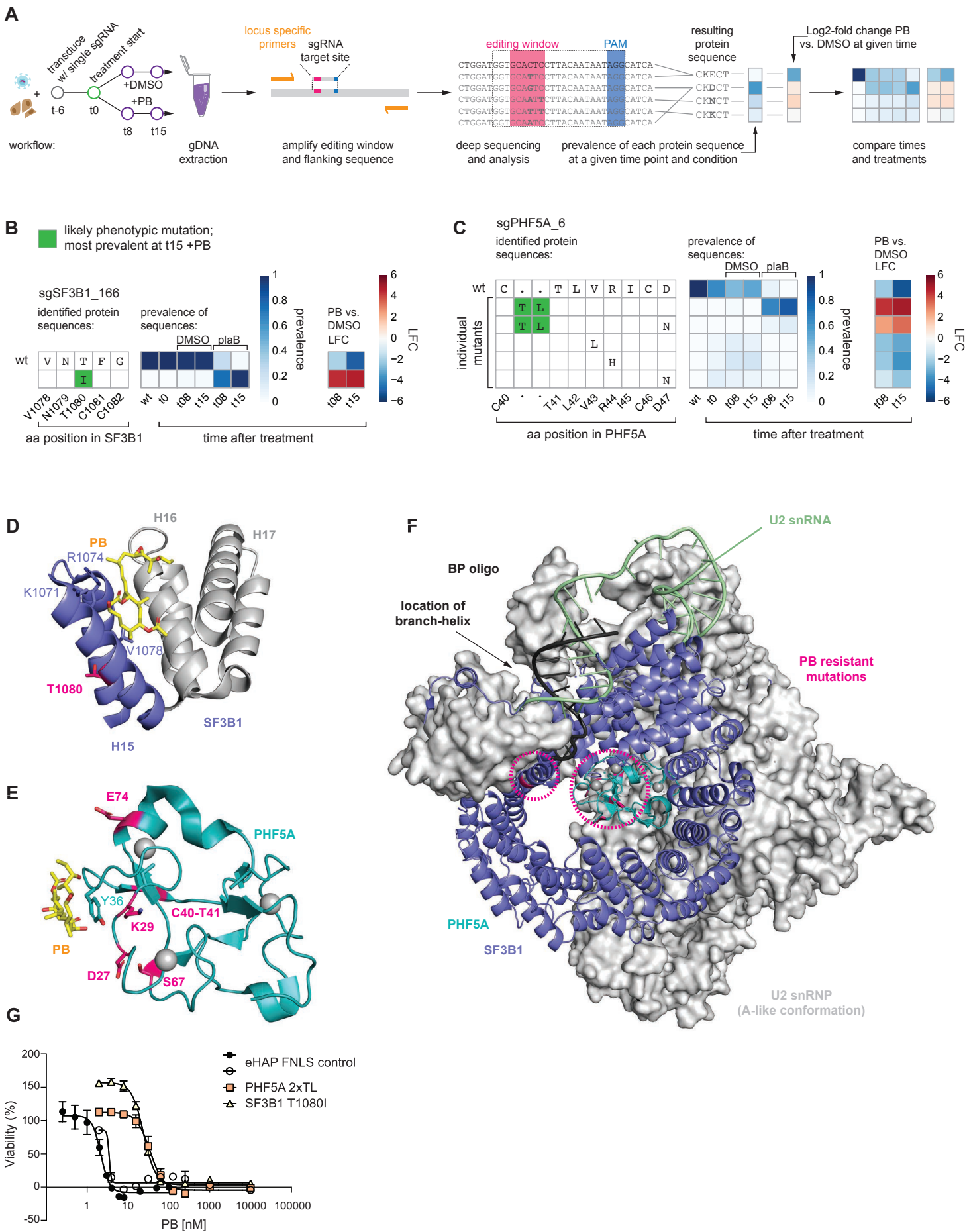


Figure 4

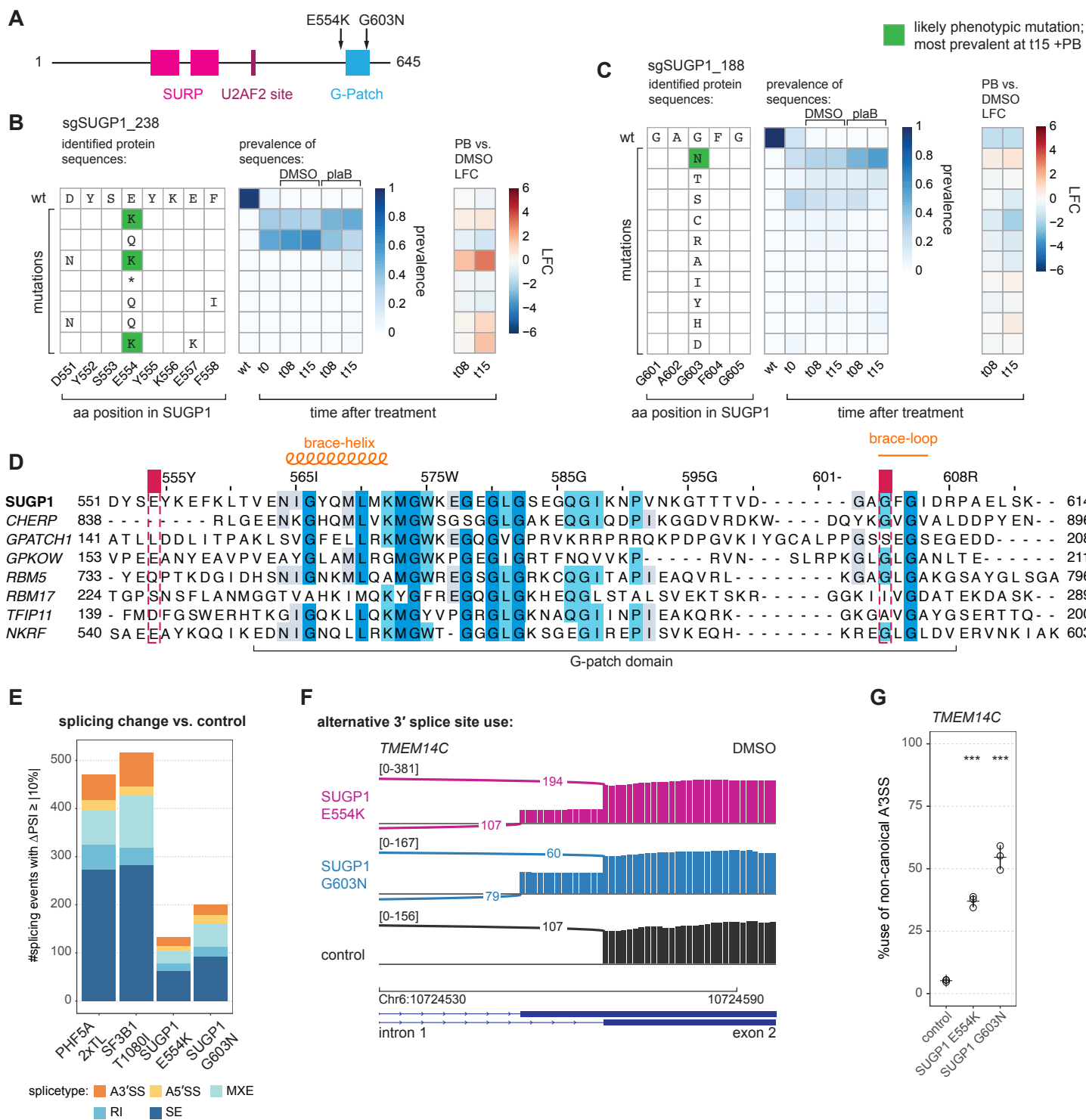


Figure 5

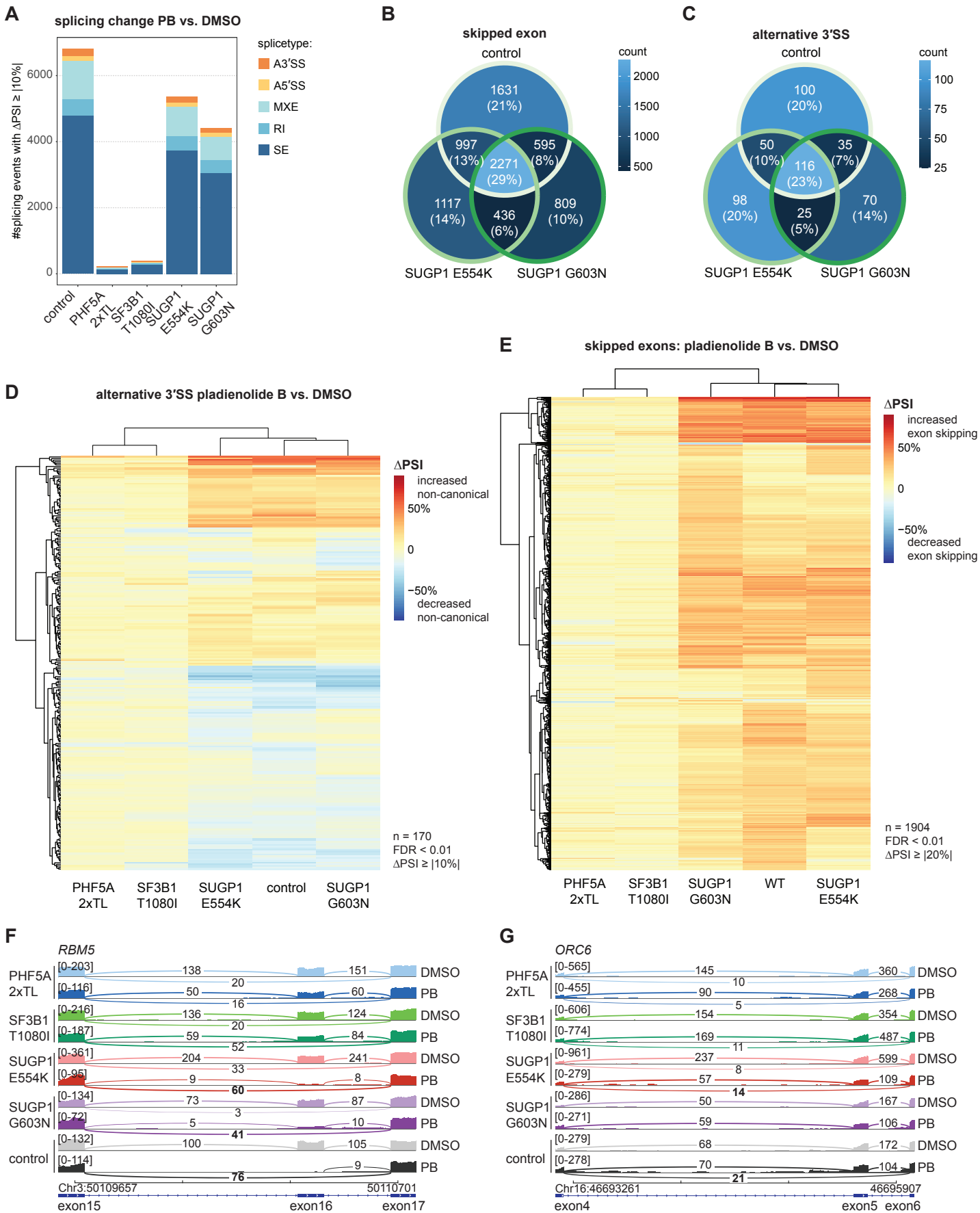


Figure 6

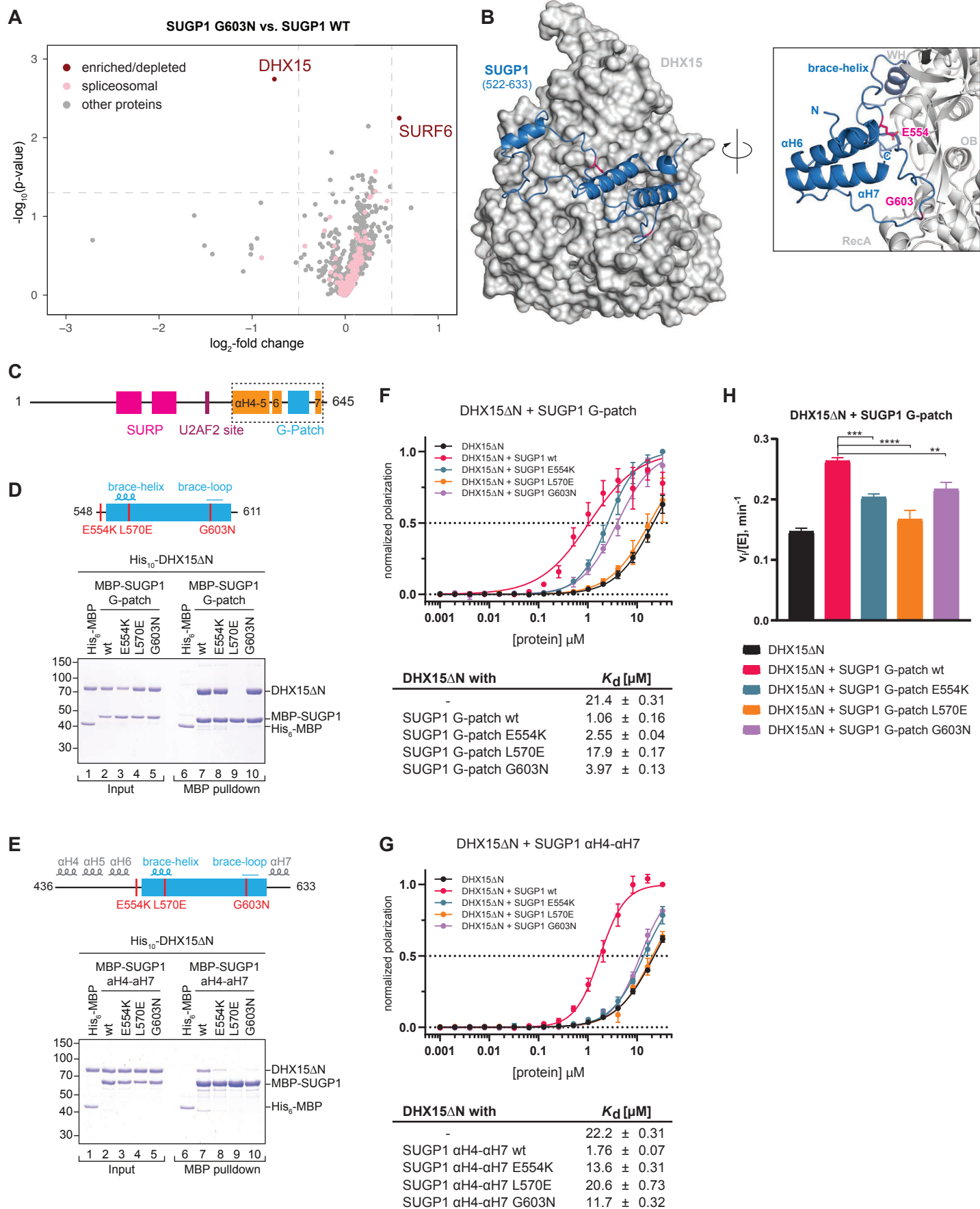


Figure 7

